Cell type-specific *cis*-regulatory divergence in gene expression and chromatin accessibility revealed by human-chimpanzee hybrid cells

Ban Wang[1,*], Alexander L. Starr[1,*], Hunter B. Fraser[1,2]

*Indicates equal contribution

1. Department of Biology, Stanford University, Stanford, CA, USA

2. Correspondence: hbfraser@stanford.edu

Abstract:

Although gene expression divergence has long been postulated to be the primary driver of human evolution, identifying the genes and genetic variants underlying uniquely human traits has proven to be quite challenging. Theory suggests that cell type-specific *cis*-regulatory variants may fuel evolutionary adaptation due to the specificity of their effects. These variants can precisely tune the expression of a single gene in a single cell type, avoiding the potentially deleterious consequences of *trans*-acting changes and non-cell type-specific changes that can impact many genes and cell types, respectively. It has recently become possible to quantify human-specific *cis*-acting regulatory divergence by measuring allele-specific expression in human-chimpanzee hybrid cells—the product of fusing induced pluripotent stem (iPS) cells of each species *in vitro*. However, these *cis*-regulatory changes have only been explored in a limited number of tissues and cell types. Here, we quantify human-chimpanzee *cis*-regulatory divergence in gene expression and chromatin accessibility across six cell types, enabling the identification of highly cell type-specific *cis*-regulatory changes. We find that cell type-specific genes and regulatory elements evolve faster than those shared across cell types, suggesting an important role for

genes with cell type-specific expression in human evolution. Furthermore, we identify several instances of lineage-specific natural selection that may have played key roles in specific cell types, such as coordinated changes in the *cis*-regulation of dozens of genes involved in neuronal firing in motor neurons. Finally, using novel metrics and a machine learning model, we identify genetic variants that likely alter chromatin accessibility and transcription factor binding, leading to neuron-specific changes in the expression of the neurodevelopmentally important genes *FABP7* and *GAD1*. Overall, our results demonstrate that integrative analysis of *cis*-regulatory divergence in chromatin accessibility and gene expression across cell types is a promising approach to identify the specific genes and genetic variants that make us human.

Introduction:

In the past few million years, humans have evolved a multitude of unique phenotypes (Shave et al., 2019; Vanderhaeghen & Polleux, 2023). For example, our cardiovascular system has evolved to enable extended periods of physical exertion and the unique aspects of our nervous system enable human language and toolmaking (Shave et al., 2019; Vanderhaeghen & Polleux, 2023). Previous research suggests that much of human adaptation may be caused by changes in gene expression (Fraser, 2013; King & Wilson, 1975; Reilly & Noonan, 2016; Romero et al., 2012). To catalog these changes, studies have compared gene expression in post-mortem tissues of humans and our closest living relatives, chimpanzees (Blake et al., 2020; Kelley & Gilad, 2020; Ma et al., 2022). Although thousands of differentially expressed genes have been identified in post-mortem samples, it is generally not possible to determine whether genetic differences cause a gene to be differentially expressed. In post-mortem studies, genetic differences cannot be disentangled from sources of variation such as differences in diet, environment, cell type abundances, age, post-mortem interval, and other confounding factors. In addition, for many traits the relevant gene expression differences may be specific to early development,

49 but it is impossible to study fetal development *in vivo* in non-human great apes due to both ethical and
50 technical difficulties. To circumvent these issues, several groups have used great ape iPS cells to study
51 differences in gene expression in cell types present in early development (Benito-Kwiecinski et al., 2021;
52 Field et al., 2019; Kanton et al., 2019; Pavlovic et al., 2018). While the use of iPS cells addresses many of
53 the confounding factors present in post-mortem comparisons, they also introduce new issues such as
54 interspecies differences in iPS cell differentiation kinetics, efficiency, and maturation. Overall, it remains
55 tremendously challenging to identify human-specific changes in gene expression, which limits our ability
56 to link expression differences to either phenotypic differences or natural selection on the human
57 lineage.
58
59 One particularly powerful means of studying the evolution of gene expression is through the
60 measurement of allele specific expression (ASE) in hybrids between two species (Combs et al., 2018;
61 Fraser, 2011; Hu et al., 2022; Mack & Nachman, 2017; Wittkopp et al., 2004). This approach has the
62 advantage of eliminating many confounding factors inherent to interspecies comparisons, including
63 differences in cell type composition, environmental factors, developmental stage, and response to
64 differentiation protocols. Because the trans-acting environments of the two alleles in a hybrid are
65 identical, ASE has the additional benefit of reflecting only *cis*-regulatory changes, which are thought to
66 be less pleiotropic and more likely to drive evolutionary adaptation than broader *trans*-acting changes
67 (Agoglia et al., 2021; Gokhman et al., 2021; Prud'homme et al., 2007; Wittkopp & Kalay, 2012).
68 Furthermore, ASE enables the use of powerful methods that can detect lineage-specific natural selection
69 and, as a result, contribute to our understanding of the selective pressures that have shaped the
70 evolution of a wide variety of species (Fraser, 2011). Until recently, it has not been possible to
71 disentangle *cis*- and *trans*-acting changes fixed in the human lineage since humans cannot hybridize with
72 any other species. However, the development of human-chimpanzee hybrid iPS cells enables

73 measurement of ASE in a wide variety of tissues and developmental contexts (Agoglia et al., 2021;
74 Gokhman et al., 2021; Song et al., 2021). This provides an effective platform to investigate general
75 principles of hominid gene expression evolution, detect lineage-specific selection, and identify candidate
76 gene expression changes underlying human-specific traits.
77
78 While gene expression differences between humans and chimpanzees are well-studied, there has been
79 less focus on epigenetic changes, many of which are likely to underlie differences in gene expression
80 (García-Pérez et al., 2021; Kozlenkov et al., 2020; Netherlands Brain Bank et al., 2016; Trizzino et al.,
81 2017). Furthermore, these studies, regardless of whether they utilize post-mortem tissues or cell lines,
82 are subject to the same confounding factors mentioned above. Analogous to ASE, one can use the assay
83 for transposase accessible chromatin using sequencing (ATAC-seq) in interspecies hybrids to measure
84 allele-specific chromatin accessibility (ASCA) (Buenrostro et al., 2013; Corces et al., 2017; Liang et al.,
85 2021; S. Zhang et al., 2020). As with ASE, ASCA is unaffected by many confounders inherent to between-
86 species comparisons and only measures *cis*-regulatory divergence. Perhaps most importantly, ASCA can
87 implicate specific regulatory elements that likely underlie gene expression differences. These regulatory
88 elements can then be more closely studied to identify the likely causal genetic variants and the
89 molecular mechanisms by which those variants alter gene expression.
90
91 Here, we generated RNA-seq and ATAC-seq data from six human-chimpanzee hybrid iPS cell-derived cell
92 types and quantified ASE and ASCA. Using this dataset, we identified thousands of genes and *cis*-
93 regulatory elements showing cell type-specific ASE and ASCA. We found that cell type-specific genes and
94 *cis*-regulatory elements are more likely to have divergent expression and accessibility than their more
95 broadly expressed/accessible counterparts. Furthermore, we provide evidence for polygenic selection
96 on the expression level of genes associated with physiologically relevant gene sets including sodium

97 channels and syntaxin-binding proteins in motor neurons. Finally, we use newly developed metrics and
98 machine learning algorithms to link cell type-specific differences in chromatin accessibility and gene
99 expression and identify putative causal mutations underlying these differences. Using this pipeline we
100 identified motor neuron-specific increases in promoter chromatin accessibility and gene expression for
101 *FABP7*, which plays a key role in neurodevelopment but is not well-studied in neurons. In addition, we
102 focus on a human-accelerated region (HAR) near the promoter of *GAD1*. While this region is accessible
103 in all cell types, both the accessibility of the HAR and the expression of *GAD1* are only chimpanzee-
104 biased in motor neurons. Analysis of scRNA-seq from human and chimpanzee brain organoids showed
105 that increased expression of *GAD1* also occurs in ventral forebrain inhibitory neurons. Overall, this study
106 provides insight into the evolution of gene expression in great apes as well as a resource that will inform
107 functional dissection of human-specific molecular changes.
108
109 **Results**
110
111 **Cis-regulatory divergence of gene expression in six cell types is largely cell type-specific or shared**
112 **across all cell types**
113
114 To measure genome-wide cis-regulatory divergence in gene expression, we performed RNA-seq on six
115 cell types derived from human-chimpanzee hybrid iPS cells (Fig. 1a). The cell types profiled were from six
116 diverse developmental lineages including the motor neuron (MN), cardiomyocyte (CM), hepatocyte
117 progenitor (HP), pancreatic progenitor (PP), skeletal myocyte (SKM), and retinal pigment epithelium
118 (RPE) lineages. These represent all three germ layers and a variety of organs (Fig. 1a). It is worth noting
119 that these differentiations do not necessarily lead to a pure population of cells, but rather a population
120 of cells with different levels of maturity along a particular developmental lineage. For example, the SKM

121 population likely contains fully differentiated muscle fibers as well as a small population of proliferating
122 satellite cells; for clarity we refer to this as the SKM cell type. As these different cell types are not shared
123 between tissues, we use cell type-specific and tissue-specific interchangeably throughout the
124 manuscript.
125
126 Two independently generated hybrid lines were differentiated for each cell type and at least two
127 biological replicates per hybrid line per cell type were collected (see Methods). Each cell type was
128 sequenced to an average depth of 134 million paired-end reads (Supp Fig. 1). We used a computational
129 pipeline to quantify ASE adapted from the pipeline introduced by Agoglia et al (Agoglia et al., 2021).
130 Briefly, we computed ASE by mapping reads to both the human and chimpanzee genomes, correcting
131 for mapping bias, and assigning reads to the human or chimpanzee genome if a read contained one or
132 more human-chimpanzee single nucleotide differences (see Methods).
133
134 As expected, the samples clustered predominantly by cell type (Fig. 1b-c). Within four of the six cell type
135 clusters, individual samples clustered by line rather than species of origin, potentially indicating line to
136 line variability in differentiation (Fig. 1b). This highlights the importance of measuring ASE which, by
137 definition, is measured within each line and so robust to variability between lines. Indeed, when
138 performing PCA within cell types using allelic counts (i.e. counting reads from the human allele and
139 chimpanzee allele separately), human and chimpanzee species differences were clearly separated by
140 principal component (PC) 1 or PC2 in each cell type (Fig. 1d, Supp Fig. 2). To assess the success of our
141 differentiations, we examined each cell type for the expression of known marker genes in our RNA-seq
142 data (Fig. 1e, Supp Fig. 3). All cell types express canonical marker genes and do not express pluripotency
143 markers, indicating that the differentiations were successful (Fig. 1e, Supp Fig 3, Additional file 1)

144 (Burridge et al., 2014; Chal et al., 2016; Korytnikov & Nostro, 2016; Mallanna & Duncan, 2013; Maury et
145 al., 2015; Sharma et al., 2019).
146
147 Because our hybrid cells were grown concurrently with their human and chimpanzee diploid "parental"
148 cells, we performed an additional check for purity of the hybrid lines by quantifying genome-wide ASE.
149 We noticed that among our 25 RNA-seq samples, the two PP hybrid2 samples had a slight bias towards
150 higher expression from the chimpanzee alleles across all chromosomes. This is likely due to a small
151 fraction of contaminating chimpanzee cells in these samples. We corrected for this by reducing the
152 chimpanzee allele counts such that the number of reads assigned to the human and chimpanzee alleles
153 was equal. By simulating contamination of a hybrid sample with chimpanzee cells, we found that this
154 correction was conservative and that the log fold-change estimates were largely unaffected by
155 contamination after this correction (Methods, Supp Fig. 4).
156
157 We next investigated which genes were differentially expressed between the human and chimpanzee
158 allele in each cell type (Fig. 2a). We identified thousands of genes showing significantly biased ASE in
159 each cell type at a false discovery rate (FDR) cutoff of 0.05 (Fig. 2b). We detected a comparable number
160 of ASE genes in all cell types except SKM. As a result, we repeated all subsequent analyses both including
161 and excluding SKM and obtained qualitatively similar results regardless of whether SKM was included.
162
163 While a considerable number of genes had significant ASE in all cell types, many more genes only had
164 significant ASE in a single cell type, suggesting cell type-specific *cis*-regulatory divergence (Fig. 2b). A
165 notable family of developmentally important genes that exemplifies differences in ASE across cell types
166 is the neurotrophins and their receptors (Fig. 2c) (Caporali & Emanueli, 2009; Huang & Reichardt, 2001).
167 For example, *NTRK3*, which plays a key role in the development of the nervous system, is only

168 differentially expressed in RPE and MN but is chimpanzee-biased in RPE and human-biased in MN (Supp
169 Fig. 5) (Ichim et al., 2012; Naito et al., 2017). In addition, the gene coding for its primary ligand (*NTF3*) is
170 differentially expressed in a variety of cell types yet is human-biased in all cell types except MN in which
171 it is chimpanzee-biased (Supp Fig. 5). *NTRK1* differential expression is similarly tissue-specific as it is
172 strongly chimpanzee-biased in MN, but human-biased in CM and SKM (Supp Fig. 5). These results
173 indicate that the regulatory landscape of these genes has undergone many complex *cis*-regulatory
174 changes as the human and chimpanzee lineages have diverged.
175
176 To further investigate the relationship between tissue-specificity and ASE, we asked whether genes with
177 variable expression across tissues are more likely to show ASE. Using a standard definition of cell type-
178 specific genes—those with detectable expression in only one cell type in our study—we found that cell
179 type-specific genes were typically enriched for ASE in the one cell type where they are expressed (Supp
180 Fig. 6) (GTEx Consortium, 2017; Jain & Tuteja, 2019). However, other cell type-specific expression
181 patterns such as uniquely low expression in a particular cell type may also indicate an important dosage-
182 sensitive function in that cell type. We therefore focused on a broader definition of cell type-specificity
183 in which genes that are differentially expressed between one cell type and all others in our study (FDR <
184 0.05 for each pairwise comparison) are considered cell type-specific for that cell type. We found that
185 this more inclusive definition, which assigned many more genes to be cell type-specific, showed an even
186 more significant ASE enrichment than the narrower definition (Fig. 2d). This result is not sensitive to the
187 choice of FDR cutoff nor driven solely by a subgroup of highly expressed genes as it is well-preserved
188 across FDR cutoffs (Supp Fig. 7) and different gene expression levels (Supp Fig. 8). This trend is also
189 robust to separating samples into two groups and using one to define cell type-specific genes and the
190 other to identify differentially expressed genes. This controls for spurious relationships that can result

191 when the same data are used to define two different quantities which are then compared (Supp Fig. 9)
192 (Fraser, 2019).
193
194 This enrichment (Fig. 2d) suggests that tissue-specific genes may have less constraint and/or more
195 frequent positive selection on their expression. We reasoned that if the trend was solely driven by
196 constraint, then controlling for constraint—even if imperfectly—would be expected to reduce the
197 strength of the relationship. To investigate this, we binned genes by their variance in ASE across a large
198 cohort of human samples which we have previously shown acts as a reasonable proxy for evolutionary
199 constraint on gene expression (Castel et al., 2020; Starr et al., 2023). Across cell types, we generally
200 observe significant enrichments in each bin and little difference in enrichment between bins, suggesting
201 that differences in constraint on expression of cell type-specific vs. ubiquitously expressed genes are not
202 solely responsible for our observations (Supp Fig. 10). Furthermore, we observe even stronger
203 enrichments using an alternative constraint metric, the probability of haploinsufficiency score (pHI)
204 likely due to the larger number of genes for which pHI can be calculated (Supp Fig. 11) (Collins et al.,
205 2022). Overall, our analysis suggests that differences in constraint are unlikely to fully explain these
206 trends, suggesting a potential role for positive selection.
207
208 **Lineage-specific selection has acted on tissue-specific gene expression divergence**
209
210 Next, we sought to use our RNA-seq data to identify instances of lineage-specific selection. We used a
211 previously published method that incorporates a tissue-specific measure of constraint on gene
212 expression to test whether groups of genes have likely been under selection (Starr et al., 2023). Using
213 this strategy, we detected several signals of putative lineage-specific selection, some of which were cell
214 type-specific (Additional file 2). Notably, the four most significant enrichments were found in motor

215 neurons and cardiomyocytes and are highly relevant to those cell types (Fig. 2e; Additional file 2). In
216 cardiomyocytes, the top pathway was “PPAR signaling pathway” which has been shown to play an
217 important role in the regulation of heart morphology and lipid metabolism (Montaigne et al., 2021). For
218 example, *NR1H3* (also known as *LXRA*) is strongly upregulated in human cardiomyocytes as well as all
219 other cell types (Supp Fig. 12a). Furthermore, this upregulation appears to have occurred in the human
220 lineage based on data from non-hybrid cardiomyocytes as well as adult hearts (Supp Fig. 12b) (Blake et
221 al., 2020; Pavlovic et al., 2018). Hybrid cells are essential in determining that the human-specific
222 upregulation of *NR1H3* in cardiomyocytes has a strong genetic component as *NR1H3* expression is very
223 responsive to diet and other environmental factors (Wang & Tontonoz, 2018).
224
225 In motor neurons, multiple categories showed a strong bias toward higher chimpanzee expression
226 including “sodium ion transmembrane transport” and “syntaxin binding”. The genes in these categories
227 are of fundamental importance to the function of motor neurons as sodium ion transporters control
228 excitability and syntaxin binding proteins play a major role in controlling the release of
229 neurotransmitters from synaptic vesicles (Brose et al., 2019; Meisler et al., 2021). Interestingly, several
230 key genes in these sets appear to have human-derived differences in expression that extend beyond
231 motor neurons to other neuronal types. For example, *SCN1B, SCN2B,* and *SYT2* have chimpanzee-biased
232 ASE in our MN data. Similarly, these genes have human-biased expression when comparing human,
233 chimpanzee, and rhesus macaque glutamatergic cortical neurons in a previously published dataset (Supp
234 Fig. 13) (Kozlenkov et al., 2020). We note that several other genes in these genes sets are not
235 differentially expressed between humans and chimpanzees in this cortical neuron dataset, emphasizing
236 the importance of studying individual neuron types (Kozlenkov et al., 2020). Overall, the strong bias in
237 gene expression of sodium ion transporters and syntaxin binding proteins we observe suggests lineage-
238 specific selection that may have altered the electrophysiological properties of human motor neurons.

239

240 **Patterns of allele-specific chromatin accessibility reveal divergent *cis*-regulatory elements**

241

242 While ASE provides insight into what gene expression changes might underlie phenotypic differences
243 between humans and chimpanzees, in the absence of additional data it is very difficult to prioritize
244 which specific mutations might cause expression divergence. To begin to fill this gap, we generated
245 ATAC-seq data from five of the six cell types (all except RPE), with each cell type sequenced to an
246 average depth of 184 million paired-end reads (Supp Fig. 14). ATAC-seq uses a hyperactive Tn5
247 transposase to cleave DNA that is not bound by nucleosomes to enrich for accessible chromatin (Fig. 3a),
248 a hallmark of active *cis*-regulatory elements (CREs) (Buenrostro et al., 2013; Corces et al., 2017). We
249 estimated ASCA for individual open chromatin peaks by mapping reads to both species' reference
250 genomes, correcting for mapping bias, generating a unified list of peaks across all samples, and then
251 counting reads supporting each allele in each peak (see Methods). Cell types clustered well using PC1
252 and PC2 of the ATAC-seq data, except for the HP sample which clustered closely with PP samples (Fig.
253 3b, Supp Fig. 15). However, performing PCA on just the HP and PP samples clearly separates the two cell
254 types (Supp Fig. 16). Within each cell type, species differences were clearly separated by PC1 or PC2
255 (Supp Fig. 17). As an example of ASCA, the accessibility of the promoter of *CTSF* was strongly
256 chimpanzee-biased, mirroring the chimpanzee-biased ASE for this gene (Fig. 3c).

257

258 As a first step in analyzing the ATAC-seq data, we intersected the peaks we identified with the genomic
259 annotations of chromatin states. These fifteen categories, predicted across many tissues and cell types
260 by the chromHMM model (Vu & Ernst, 2022), include terms such as "TSS" (transcription start site) and
261 "enhancer". We then plotted the median of the absolute human-chimpanzee ASCA log fold-changes for
262 each chromatin state and cell type (Fig 3d). The TSS and promoter annotations were the least divergent

263 in their accessibility, whereas regions of heterochromatin were the most divergent (Fig. 3d). To explore
264 the relationship between interspecies differences in ASCA and ASE, we assigned peaks to the nearest
265 TSS and computed the Pearson correlation between the allelic log fold-change of chromatin accessibility
266 and expression within each cell type and chromatin state. As expected, TSS and promoter annotations
267 showed the strongest correlation between ASCA and ASE, and correlations were stronger when
268 including only differentially accessible peaks (Fig. 3e, Methods). Intriguingly however, ASCA of regions
269 annotated as heterochromatin, polycomb repressed, or quiescent were as strongly correlated with ASE
270 as elements identified as enhancers or DNase hypersensitivity sites (Fig. 3e). Notably this result is robust
271 to how peaks and chromHMM annotations were intersected (Supp Fig. 18a), as well as to removal of all
272 peaks even slightly overlapping TSS or promoter-related annotations (Supp Fig. 18b). Given that
273 heterochromatin/quiescent regions are highly divergent in ASCA (Fig. 3d), this suggests that changes in
274 accessibility of these regions may be particularly important in the evolution of gene expression.
275
276 Next, we investigated whether the analog of the relationship between cell type-specific gene expression
277 and ASE (Fig. 2d) holds for chromatin accessibility. Since the number of called peaks is largely dependent
278 on sequencing depth (Supp Fig. 14, 19a), we performed down-sampling to equalize power to detect
279 peaks across cell types (Supp Fig. 19b, Methods). We then called peaks on the down-sampled data and
280 identified peaks as cell type-specific if they were called as peaks in only one cell type. In agreement with
281 the gene expression data, we observed that cell type-specific peaks are enriched for ASCA across all cell
282 types and this enrichment generally holds when using varying $\log_2$ fold-change or p-value cutoffs (Supp
283 Figs. 20-21). Analogous to our analysis of gene expression, we also applied a broader definition of cell
284 type-specificity to the ATAC data, in which a peak was considered specific to a cell type if that peak had
285 an absolute $\log_2$ fold-change greater than a chosen threshold (e.g. 0.5 or 1) across all pairwise
286 comparisons with other cell types. We observe strong enrichment for ASCA in cell type-specific peaks

287 using this definition except when using the most stringent cutoffs due to the very low number of peaks
288 meeting these criteria (Supp Figs. 22-23, Methods). Finally, we observe the same enrichments when
289 controlling for a recently published metric for constraint on non-coding elements, suggesting that
290 differences in evolutionary constraint may not be solely responsible for the observed trends (Supp Fig.
291 24) (S. Chen et al., 2022).
292
293 We next explored the relationship between cell type-specific ASCA and ASE. To do this, we developed a
294 novel metric called differential expression enrichment (dEE) to quantify how specific the log fold-change
295 is to a particular cell type or tissue. Our method is based on expression enrichment (EE) (Yu et al., 2006),
296 a metric that measures how specific gene expression is to a certain cell type/tissue. dEE estimates how
297 cell type-specific ASE is for a gene (Supp Fig. 25, Methods) and, analogously, dCAE (differential
298 chromatin accessibility enrichment) measures how cell type-specific ASCA is for a *cis*-regulatory element
299 (Supp Fig. 26, Methods). dEE and dCAE are high in a cell type if there is a high absolute log fold-change in
300 that cell type and much lower absolute log-fold changes or log fold-changes in the opposite direction in
301 the other cell types. For example, dEE would be close to one for a gene in a cell type if the gene had
302 strongly human-biased ASE in that cell type and very weakly human-biased or chimpanzee-biased ASE in
303 the other cell types. On the other hand, if a gene did not have any strong allelic bias, that gene would
304 have dEE close to zero. dEE is conceptually related to a metric we have previously introduced, diffASE,
305 and generalizes diffASE to an arbitrary number of cell types and any assay that produces log fold-
306 changes (Combs et al., 2018; Hu et al., 2022; York et al., 2018). Using these metrics, we identified 154
307 instances in which a gene with cell type-specific ASE (i.e., high dEE) had a peak with cell type-specific
308 ASCA in the same cell type (i.e., high dCAE, see Additional file 3 for the full list). Of these, 95 showed
309 ASCA and ASE in the same direction which is more than expected by chance (77 expected; $p < 0.005$,
310 binomial test). These results suggest that tissue-specific *cis*-regulatory divergence in chromatin

311 accessibility may often impact tissue-specific gene expression, though this divergence is neither
312 necessary nor sufficient to do so.
313
314 **Identifying candidate causal *cis*-regulatory variants by integrating ASE and ASCA across cell types**
315
316 As high dEE and dCAE in a given cell type might be indicative of a causal link between the change in
317 chromatin accessibility and the change in expression, we focused on the 95 peak-gene pairs with
318 matching direction and used two different strategies to identify examples to investigate in detail. First,
319 we prioritized genes known to play important roles in development. For example, we found that the
320 promoter of *FABP7* has human-biased ASCA specifically in motor neurons (Fig. 4a-b) and that the *FABP7*
321 gene has human-biased ASE in motor neurons (Fig 4c). *FABP7* is used as a marker of glial cells and neural
322 progenitor cells (NPCs) and plays a key role in NPC proliferation and astrocyte function (Arai et al., 2005;
323 De Rosa et al., 2012; Ebrahimi et al., 2016; Watanabe et al., 2007). Using previously published single-
324 nucleus RNA-seq data from humans, chimpanzees, and rhesus macaques, we confirmed that *FABP7*
325 shows a human-derived up-regulation in several neuronal subtypes but not glial cells (Supp Fig. 27) (Ma
326 et al., 2022). To investigate the genetic basis of this cell type-specific divergence, we leveraged a
327 machine learning model, Sei (K. M. Chen et al., 2022), to nominate potentially causal variants in the
328 promoter of *FABP7* (see Methods). Sei is a deep neural network that takes DNA sequence as input and
329 predicts the probability that the sequence has a particular epigenetic state in a variety of cell types and
330 tissues (Fig. 4d) (K. M. Chen et al., 2022). While single-base substitutions differing between human and
331 chimpanzee had only minor impacts on predicted *cis*-regulatory activity, “chimpanizing” the human
332 sequence of the *FABP7* promoter at two small indels (by deleting one base at chr6: 122,779,291 and
333 inserting three bases at chr6: 122,779,115) was sufficient to make the Sei predictions for the
334 chimpanized human sequence closely match the predictions for the complete chimpanzee sequence

335 (Fig. 4e-g). Making only one of these changes had substantial but weaker effects in both cases,
336 suggesting that both mutations might be functionally important (Fig. 4f,g). The 1-base insertion in the
337 human lineage introduces a binding site for the neuronally expressed transcription factors GLIS2/3,
338 suggesting a potential molecular mechanism (Calderari et al., 2018; Castro-Mondragon et al., 2022; Ke
339 et al., 2015).
340
341 As another approach to ranking the 95 peaks, we searched for peaks containing human-chimpanzee
342 sequence differences in otherwise highly conserved genomic positions, since these could reflect changes
343 in selective pressure. Using PhyloP scores for 241 placental mammals (Sullivan et al., 2023) to assess
344 conservation, one of the top-ranked peaks was a putative enhancer six kilobases away from the TSS of
345 *GAD1*, which plays a key role in the synthesis of the neurotransmitter GABA (Feldblum et al., 1993).
346 Notably, part of this peak has been classified as a human accelerated region (HAR) (Girskis et al., 2021;
347 Hubisz & Pollard, 2014; Pollard et al., 2006)—a short sequence that is highly conserved in mammals yet
348 contains an unusual number of human-specific mutations. Both the accessibility in the peak and *GAD1*
349 expression are only chimpanzee-biased in motor neurons (Fig. 4a-c, Supp Fig. 28). Applying Sei to
350 estimate the predicted effect of every variant in this region, we found that a single-nucleotide
351 substitution within the HAR (chr2: 170,823,193) has by far the largest predicted cis-regulatory effect and
352 most closely matches the differences in Sei predictions between the full human and chimpanzee
353 haplotypes (Fig. 4d-g). Interestingly, this mutation is predicted to disrupt a binding site for several basic
354 helix-loop-helix transcription factors that play essential roles in neuronal differentiation such as Ascl1
355 (Supp Fig. 29) (Castro-Mondragon et al., 2022; Mizuguchi et al., 2006; Yang et al., 2017).
356
357 As *GAD1* is only highly expressed in GABAergic neurons (and was therefore lowly expressed in the cell
358 types studied here, Supp Fig. 30a), we investigated whether this reduced expression of human *GAD1*

359 also occurs in cortical organoids which contain GABAergic neurons together with other cell types in
360 which *GAD1* is not highly expressed. We analyzed our previously published data from human-
361 chimpanzee hybrid cortical organoids (Agoglia et al., 2021) and found that the expression of *GAD1* from
362 the chimpanzee allele spikes higher than that of the human allele around day 50 of hybrid cortical
363 organoid differentiation before dropping in expression over time to match the human expression level
364 (Supp Fig. 30b). Because ASE in the hybrid cells controls for any potential interspecies differences in
365 differentiation kinetics or cell type composition, this difference must be the result of *cis*-regulatory
366 divergence between humans and chimpanzees. This expression difference is also more pronounced in
367 comparisons of human and chimpanzee parental cortical organoids, with a higher absolute log fold-
368 change at day 50, day 100, and day 150, only returning to equal expression at day 200 (Supp Fig. 30c).
369 While this could be due to differences in cell type proportion between human and chimpanzee
370 organoids, it might also be due to a reinforcing *trans*-acting effect.
371
372 To test whether this difference in expression also occurs specifically during GABAergic neuron
373 differentiation we examined *GAD1* expression in single cell RNA-seq data from human and chimpanzee
374 cortical organoids (Kanton et al., 2019). We observed a spike in *GAD1* expression in less mature
375 chimpanzee GABAergic neurons that is absent in the corresponding part of the trajectory in human
376 neurons (Supp Fig. 31). Notably, a similar trend holds regardless of which GABAergic sub-trajectory (i.e.,
377 equivalent to GABAergic neurons from the caudal, lateral, or medial ganglionic eminences) is examined
378 suggesting this difference is not unique to a particular type of GABAergic neuron (Supp Fig. 31). Finally,
379 we examined the accessibility of the putative *GAD1* enhancer more closely. Consistent with a potential
380 role for this enhancer in the spike in *GAD1* expression during development, the accessibility of this
381 enhancer mirrors the expression of *GAD1* in human cortical and striatal organoids (Supp Fig. 32) with
382 high accessibility between day 50 and day 100 before decreasing somewhat near day 150 (Trevino et al.,

383 2020). Overall, our results demonstrate how the combination of RNA-seq, ATAC-seq, and machine
384 learning models can nominate variants that may be responsible for cell type-specific changes in gene
385 expression and chromatin accessibility.
386
387 **Discussion**
388
389 In this study, we quantified human-chimpanzee *cis*-regulatory divergence in gene expression and
390 chromatin accessibility in six different cell types representing diverse developmental lineages. Across the
391 thousands of genes with ASE, we found that most *cis*-regulatory divergence is specific to one or a few
392 cell types. Furthermore, we found that divergent *cis*-regulation is linked to tissue-specificity, with tissue-
393 specific genes being enriched for ASE and tissue-specific regulatory elements being enriched for ASCA.
394 As this result was largely unchanged when stratifying by evolutionary constraint, our results suggest that
395 changes in the expression of genes with more cell type-specific expression patterns may be less
396 deleterious than changes in more broadly expressed genes, supporting the idea that cell-type specific
397 divergence may be less pleiotropic (Wittkopp & Kalay, 2012). Overall, this suggests that broad changes
398 in expression in cell type-specifically expressed genes may be an important substrate for evolution.
399
400 We also identified several sets of genes evolving under lineage-specific selection that may have played a
401 role in establishing unique facets of human physiology and behavior. Most interestingly, we found
402 evidence for selection on sodium ion transporters and syntaxin binding proteins that may alter the
403 electrophysiological properties of motor neurons, and potentially other types of neurons as well (Brose
404 et al., 2019; Meisler et al., 2021). The complexity of the molecular machinery regulating neuronal
405 excitability and synaptic vesicle release make it difficult to say what the effects of these gene expression
406 changes are on the excitability of motor neurons without electrophysiology data from human and great

407 ape neurons coupled with perturbation of candidate genes. However, given the divergence in
408 locomotion and motor skills between humans and chimpanzees, it is tempting to speculate that these
409 changes may have had some role in the evolution of motor control and learning in humans.
410
411 In this work, we developed two metrics—dEE and dCAE—to quantify the degree of cell type-specific
412 differential expression and accessibility. These metrics are largely analogous to widely used metrics that
413 quantify tissue- or cell type-specific expression level and applicable to any comparison of log fold-
414 changes across conditions. They markedly improved our ability to identify matching cell type-specific
415 ASE and ASCA and led to the identification of 95 peak-gene pairs that had highly cell type-specific
416 concordant changes in accessibility and expression.
417
418 One such example is a potentially human-derived increase in *FABP7* expression in several types of
419 human neurons. As *FABP7* is not highly expressed in adult mouse neurons, the functional consequences
420 of its higher expression in human neurons are difficult to predict (Yao et al., 2021). *FABP7* plays a role in
421 the uptake of the fatty acid Docosahexaenoic Acid (DHA), an important component of neuronal
422 membranes (Akbar et al., 2005; Choi et al., 2021). DHA promotes neuronal survival through
423 phosphatidylserine accumulation, so it is possible that the human-specific *FABP7* expression increases
424 neuronal DHA uptake leading to reduced apoptosis in human neurons during development and
425 ultimately contributing to a larger number of neurons in humans (Akbar et al., 2005; Choi et al., 2021).
426
427 In addition, we identified a highly conserved developmentally dynamic enhancer near *GAD1* that may
428 have partially lost activity in the human lineage resulting in a decrease in *GAD1* expression early in
429 GABAergic neuron development. By integrating with the deep learning model Sei, we identified a variant
430 that may account for the chimpanzee-biased ASCA in this region (K. M. Chen et al., 2022). Interestingly,

431 the ASE of *GAD1* was coupled with a relatively small (though significant) magnitude of ASCA. This could
432 potentially reflect divergence in transcription factor binding that leaves a “footprint” resulting in subtle
433 ASCA (Vierstra et al., 2020). Overall, our data suggest that this enhancer has lost activity in the human
434 lineage, potentially altering the expression pattern of *GAD1* during neuronal development. *GAD1* is the
435 rate-limiting enzyme for GABA synthesis so GABA levels are likely responsive to changes in *GAD1*
436 expression (Feldblum et al., 1993). GABA release has complex context-specific effects on
437 neurodevelopment making it difficult to speculate as to what the phenotypic effects of reduced GABA
438 synthesis during human neurodevelopment might be (Ben-Ari et al., 2012). However, the high
439 conservation of this *cis*-regulatory element in placental mammals implies that its human-specific
440 disruption is likely to have important neurodevelopmental effects. Careful perturbation of this enhancer
441 and *GAD1* expression in mouse models will be required to explore this further.
442
443 Overall, our study provides foundational data, insight, and computational tools that will improve our
444 understanding of cell type-specific *cis*-regulatory evolution and the role it has played in the
445 establishment of human-specific traits.
446

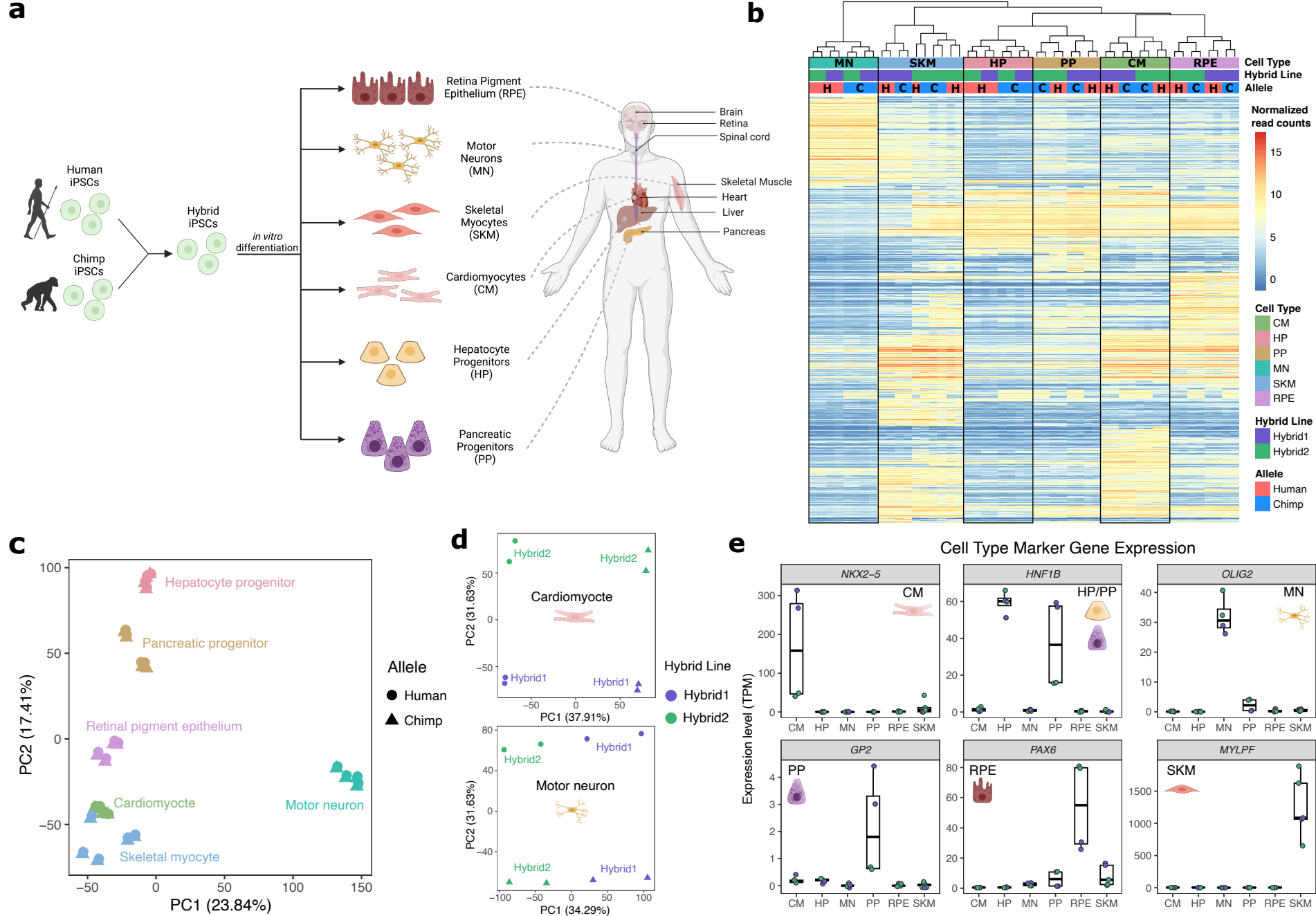
a
Human iPSCs
Chimp iPSCs
Hybrid iPSCs
in vitro differentiation
Retina Pigment Epithelium (RPE)
Motor Neurons (MN)
Skeletal Myocytes (SKM)
Cardiomyocytes (CM)
Hepatocyte Progenitors (HP)
Pancreatic Progenitors (PP)
Brain
Retina
Spinal cord
Skeletal Muscle
Heart
Liver
Pancreas
b
MN
SKM
HP
PP
CM
RPE
Cell Type
Hybrid Line
Allele
Normalized read counts
15
10
5
0
Cell Type
CM
HP
PP
MN
SKM
RPE
Hybrid Line
Hybrid1
Hybrid2
Allele
Human
Chimp
c
Hepatocyte progenitor
Pancreatic progenitor
Retinal pigment epithelium
Cardiomyocte
Motor neuron
Skeletal myocyte
PC2 (17.41%)
PC1 (23.84%)
Allele
Human
Chimp
d
Cardiomyocte
Motor neuron
Hybrid1
Hybrid2
PC2 (31.63%)
PC1 (37.91%)
PC1 (34.29%)
Hybrid Line
Hybrid1
Hybrid2
e
Cell Type Marker Gene Expression
NKX2–5
HNF1B
OLIG2
GP2
PAX6
MYLPF
CM
HP/PP
MN
PP
RPE
SKM
Expression level (TPM)
CM HP MN PP RPE SKM

446 **Figure 1: Allele-specific expression across diverse human-chimpanzee hybrid cell types. a)** Six cell types
447 were differentiated from human-chimpanzee hybrid induced pluripotent stem cells. These six cell types
448 represent diverse body systems, including motor neurons for the central nervous system, retinal
449 pigment epithelium for eye, skeletal myocytes for skeletal muscle, cardiomyocytes for the heart,
450 hepatocyte progenitors for the liver, and pancreatic progenitors for the pancreas. **b)** Heatmap showing
451 the result of hierarchical clustering performed on genes with highly variable normalized allele counts. **c)**
452 Result of running PCA on normalized allelic counts for all samples and cell types. **d)** Result of PCA
453 performed on normalized allele counts for each individual cell type separately. Cardiomyocytes and
454 motor neurons are shown here. **e)** Expression of marker genes for each cell type.

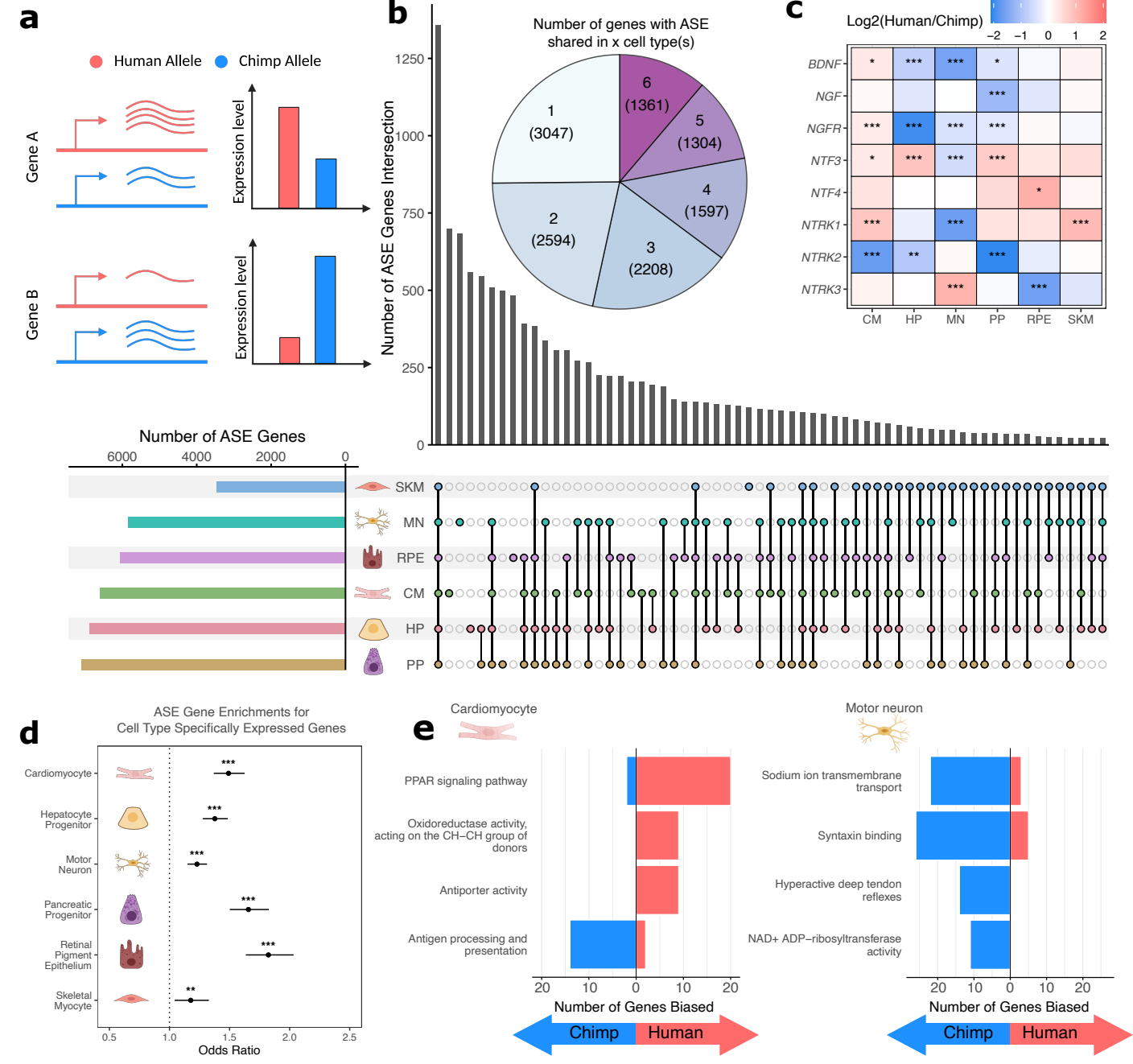
a
Human Allele
Chimp Allele
Gene A
Gene B
Expression level
Expression level
b
Number of genes with ASE shared in x cell type(s)
1 (3047)
2 (2594)
3 (2208)
4 (1597)
5 (1304)
6 (1361)
Number of ASE Genes Intersection
1250
1000
750
500
250
0
Number of ASE Genes
6000
4000
2000
0
SKM
MN
RPE
CM
HP
PP
c
Log2(Human/Chimp)
−2 −1 0 1 2
BDNF
NGF
NGFR
NTF3
NTF4
NTRK1
NTRK2
NTRK3
CM HP MN PP RPE SKM
d
ASE Gene Enrichments for Cell Type Specifically Expressed Genes
Cardiomyocyte
Hepatocyte Progenitor
Motor Neuron
Pancreatic Progenitor
Retinal Pigment Epithelium
Skeletal Myocyte
0.5 1.0 1.5 2.0 2.5
Odds Ratio
e
Cardiomyocyte
PPAR signaling pathway
Oxidoreductase activity, acting on the CH−CH group of donors
Antiporter activity
Antigen processing and presentation
20 10 0 10 20
Number of Genes Biased
Chimp
Human
Motor neuron
Sodium ion transmembrane transport
Syntaxin binding
Hyperactive deep tendon reflexes
NAD+ ADP−ribosyltransferase activity
20 10 0 10 20
Number of Genes Biased
Chimp
Human

455 **Figure 2: Human-chimpanzee ASE is largely cell type-specific. a**) Outline of measurement of allele-
456 specific expression. Reads from the human and chimpanzee alleles are counted and differences in read
457 counts identified. **b)** Thousands of genes with ASE were identified for each cell type, with many genes
458 only showing ASE in a single cell type (Conway et al., 2017). **c)** The neurotrophins and their receptors as
459 examples of genes showing cell type-specific ASE patterns. DESeq2 estimate of $\log_2$ fold-change
460 (human/chimpanzee) are shown in the heatmap and significance is indicated by asterisks where ***
461 indicates FDR < 0.005, ** indicates FDR < 0.01, and * indicates FDR < 0.05. Zero asterisks (i.e. a blank
462 box) indicates FDR > 0.05. **d)** Plot showing that genes with ASE are enriched for genes showing cell type-
463 specific expression patterns across all cell types. Asterisks indicate p-values rather than FDR using the
464 same system as in 2c. **e)** Top gene sets with evidence for lineage-specific selection in cardiomyocytes
465 and motor neurons are shown. The length of the bars indicates the number of genes in a category with
466 biased expression in each cell type.
467

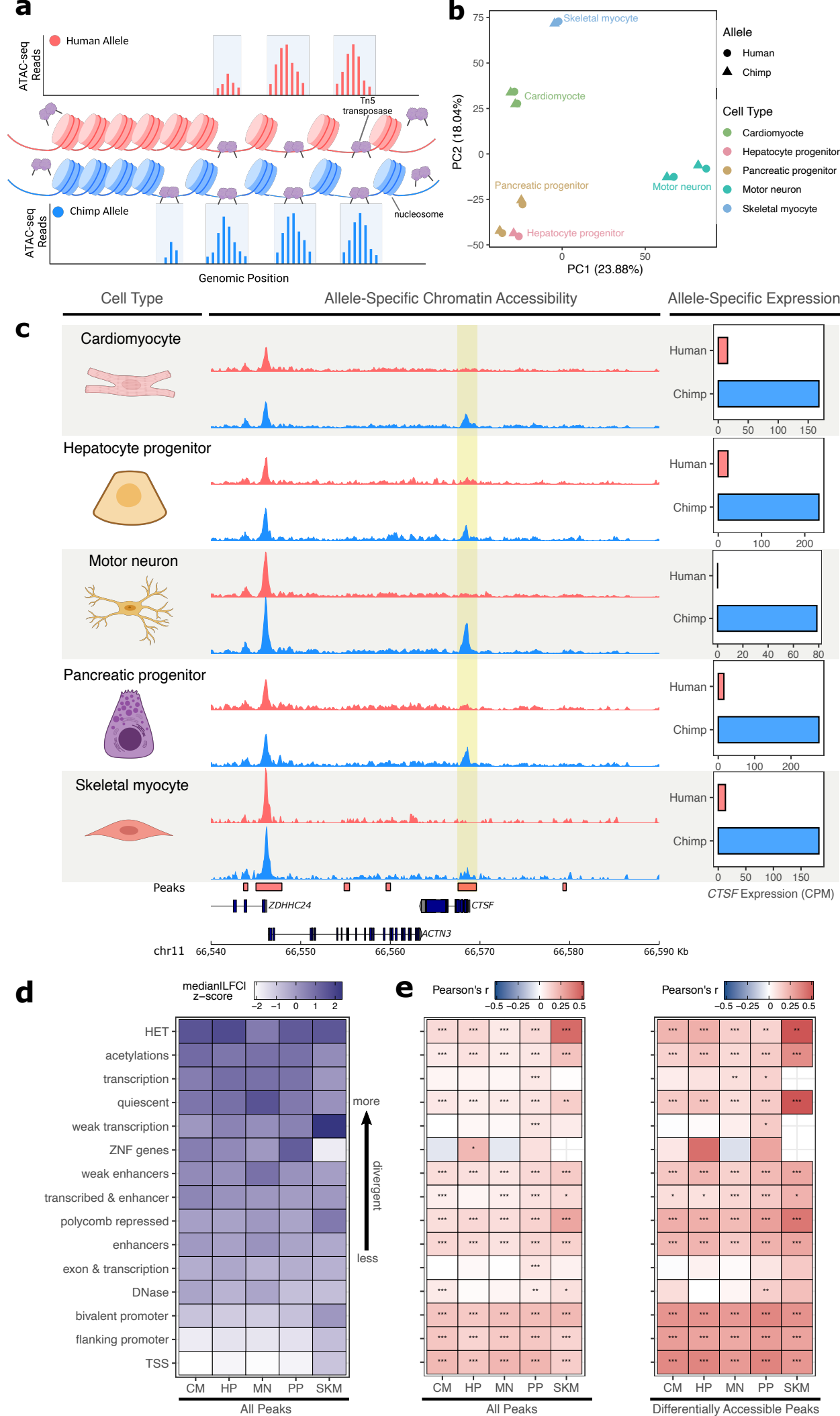
a
Human Allele
ATAC-seq Reads
Tn5 transposase
nucleosome
Chimp Allele
ATAC-seq Reads
Genomic Position
b
Skeletal myocyte
Cardiomyocte
Pancreatic progenitor
Motor neuron
Hepatocyte progenitor
PC2 (18.04%)
PC1 (23.88%)
Allele
Human
Chimp
Cell Type
Cardiomyocte
Hepatocyte progenitor
Pancreatic progenitor
Motor neuron
Skeletal myocyte
Cell Type
Allele-Specific Chromatin Accessibility
Allele-Specific Expression
c
Cardiomyocyte
Hepatocyte progenitor
Motor neuron
Pancreatic progenitor
Skeletal myocyte
Human
Chimp
Peaks
ZDHHC24
CTSF
ACTN3
chr11
66,540
66,550
66,560
66,570
66,580
66,590 Kb
CTSF Expression (CPM)
d
medianlLFCl z-score
HET
acetylations
transcription
quiescent
weak transcription
ZNF genes
weak enhancers
transcribed & enhancer
polycomb repressed
enhancers
exon & transcription
DNase
bivalent promoter
flanking promoter
TSS
more
divergent
less
CM
HP
MN
PP
SKM
All Peaks
e
Pearson's r
All Peaks
Differentially Accessible Peaks

468 **Figure 3: Allele-specific chromatin accessibility across diverse human-chimpanzee hybrid cell types. a)**
469 Schematic outlining the ATAC-seq protocol. A hyperactive transposase cleaves accessible DNA and adds
470 adapters enabling measurement of chromatin accessibility. **b)** PCA on normalized allelic counts from
471 ATAC-seq. **c)** ASCA in the promoter of *CTSF,* and ASE for the *CTSF* gene. **d)** Differences in ASCA were
472 quantified and plotted separately based on chromHMM annotation. The order is based on the median
473 of z-score transformed absolute log fold-change between human and chimpanzee across all cell types,
474 with higher z-scores indicating greater divergence in accessibility. **e)** Pearson correlation between ASE
475 and ASCA for all cell types with all peaks (left) or only differentially accessible peaks (right, defined as
476 peaks with nominal binomial p-value less than 0.05). Pearson's r values are shown in the heatmap and
477 significance is indicated by asterisks where *** indicates $p < 0.005$, ** indicates $p < 0.01$, and * indicates
478 $p < 0.05$. Zero asterisks (i.e. a blank box) indicates $p > 0.05$.
479

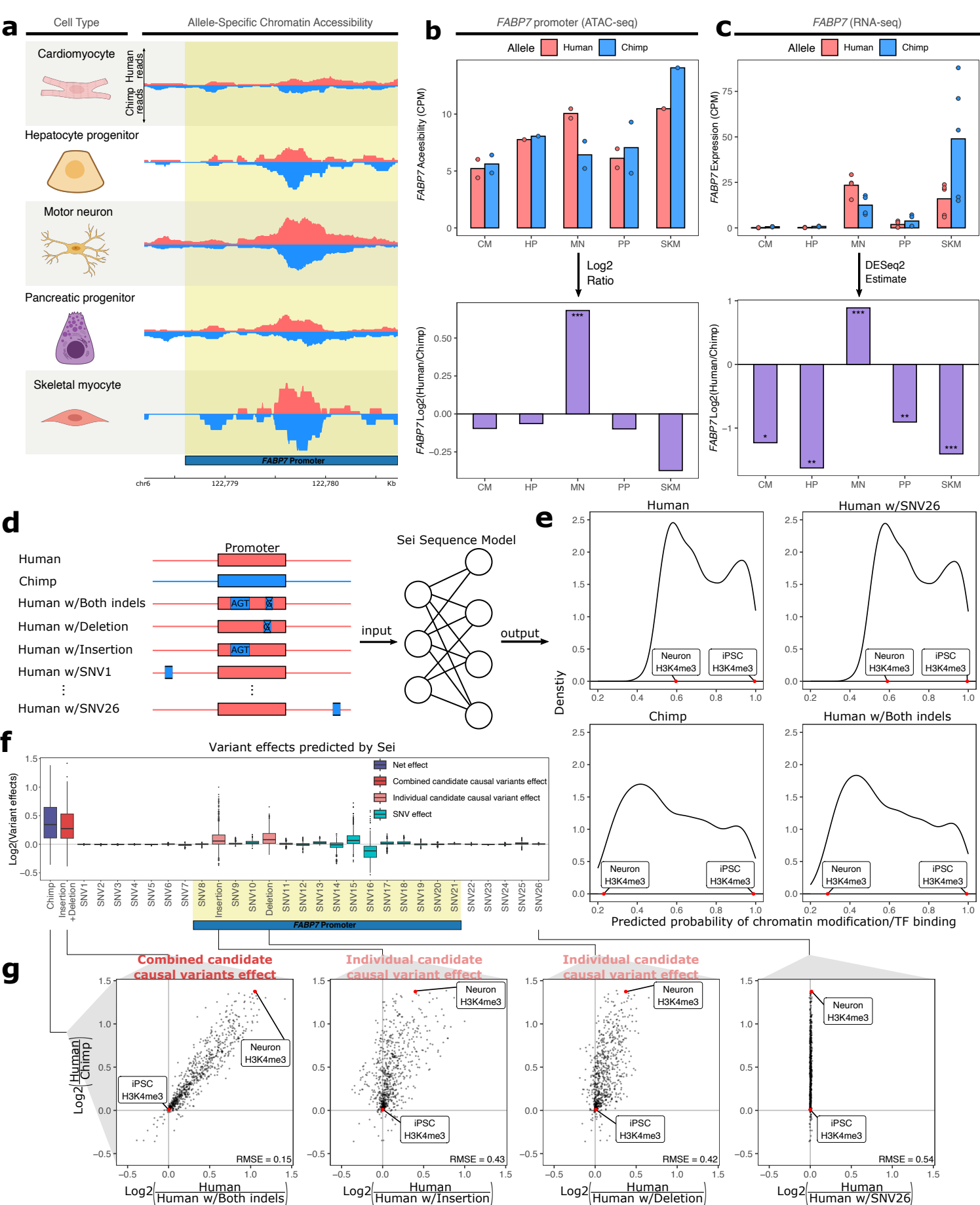
a
Cell Type
Allele-Specific Chromatin Accessibility
Cardiomyocyte
Human reads
Chimp reads
Hepatocyte progenitor
Motor neuron
Pancreatic progenitor
Skeletal myocyte
FABP7 Promoter
chr6
122,779
122,780
Kb
b
FABP7 promoter (ATAC-seq)
Allele
Human
Chimp
FABP7 Aceesibility (CPM)
CM
HP
MN
PP
SKM
Log2 Ratio
FABP7 Log2(Human/Chimp)
c
FABP7 (RNA-seq)
FABP7 Expression (CPM)
DESeq2 Estimate
d
Promoter
Human
Chimp
Human w/Both indels
Human w/Deletion
Human w/Insertion
Human w/SNV1
Human w/SNV26
AGT
input
Sei Sequence Model
output
e
Human
Human w/SNV26
Chimp
Human w/Both indels
Neuron H3K4me3
iPSC H3K4me3
Denstiy
Predicted probability of chromatin modification/TF binding
f
Variant effects predicted by Sei
Net effect
Combined candidate causal variants effect
Individual candidate causal variant effect
SNV effect
Log2(Variant effects)
Chimp
Insertion +Deletion
Insertion
Deletion
FABP7 Promoter
g
Combined candidate causal variants effect
Individual candidate causal variant effect
Individual candidate causal variant effect
Log2(Human/Chimp)
Log2(Human/Human w/Both indels)
Log2(Human/Human w/Insertion)
Log2(Human/Human w/Deletion)
Log2(Human/Human w/SNV26)
RMSE = 0.15
RMSE = 0.43
RMSE = 0.42
RMSE = 0.54

480 **Figure 4: Motor neuron-specific human-biased ASE and ASCA for *FABP7* and the promoter of *FABP7*. a)**
481 Allelic ATAC-seq tracks are shown in the peak containing the annotated *FABP7* promoter (highlighted in
482 yellow). **b)** The top panel shows allelic CPM of the *FABP7* promoter across cell types and the bottom
483 panel shows the log fold-change across cell types. **c)** The top panel shows allelic CPM of the *FABP7* gene
484 across cell types and the bottom panel shows the log fold-change across cell types. **d)** Outline of the
485 process for variant effect prediction with Sei for *FABP7*. All sequences input to Sei were centered at the
486 *FABP7* promoter. The human sequence, chimpanzee sequence, and partially "chimpanized" human
487 sequences (modified by systematically switching the human allele to the chimpanzee allele separately
488 for each human-chimpanzee difference) were fed into Sei to predict the effects of these variants on
489 chromatin state. **e)** Histogram of the probabilities of various chromatin states and transcription factor
490 binding predicted by Sei was plotted for the human sequence, the chimpanzee sequence, and the
491 human sequence with one human-chimpanzee difference swapped to match the chimpanzee sequence.
492 The human sequence with SNV26 changed to the chimpanzee allele and the human sequence switched
493 at both indels are shown as examples. A histone modification (H3K4me3) predicted in two cell types was
494 labeled to illustrate how the predictions depend on both input sequence and cell type. **f)** Plot of the
495 predicted effects of all single nucleotide differences and indels between the human and chimpanzee
496 genomes in the Sei input window (the *FABP7* promoter is highlighted in yellow). **g)** Scatterplots showing
497 the correlation of the effects of both indels (left panel), each individual indel (middle two panels), and a
498 representative SNV (right panel) on Sei predictions with the difference in Sei predictions between the
499 human and chimpanzee sequences. The root mean square error (RMSE) was computed and shown in
500 each figure.
501

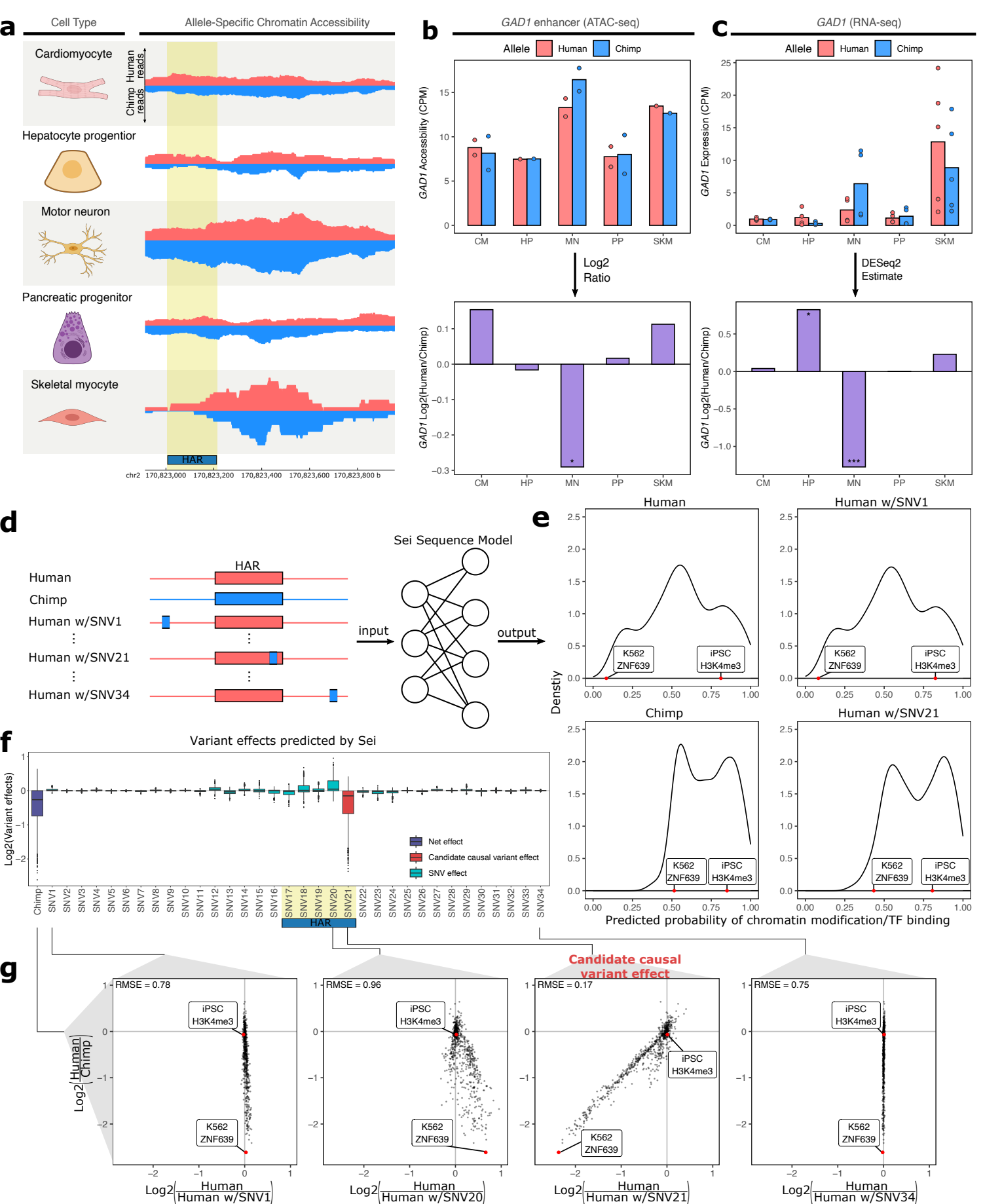
a
Cell Type
Allele-Specific Chromatin Accessibility
Cardiomyocyte
Human reads
Chimp reads
Hepatocyte progenitor
Motor neuron
Pancreatic progenitor
Skeletal myocyte
HAR
chr2 170,823,000 170,823,200 170,823,400 170,823,600 170,823,800 b
b
GAD1 enhancer (ATAC-seq)
Allele Human Chimp
GAD1 Accessibility (CPM)
CM HP MN PP SKM
Log2 Ratio
GAD1 Log2(Human/Chimp)
c
GAD1 (RNA-seq)
GAD1 Expression (CPM)
DESeq2 Estimate
d
HAR
Human
Chimp
Human w/SNV1
Human w/SNV21
Human w/SNV34
input
Sei Sequence Model
output
e
Human
Human w/SNV1
Chimp
Human w/SNV21
Denstiy
K562 ZNF639
iPSC H3K4me3
Predicted probability of chromatin modification/TF binding
f
Variant effects predicted by Sei
Log2(Variant effects)
Net effect
Candidate causal variant effect
SNV effect
Chimp SNV1 SNV2 SNV3 SNV4 SNV5 SNV6 SNV7 SNV8 SNV9 SNV10 SNV11 SNV12 SNV13 SNV14 SNV15 SNV16 SNV17 SNV18 SNV19 SNV20 SNV21 SNV22 SNV23 SNV24 SNV25 SNV26 SNV27 SNV28 SNV29 SNV30 SNV31 SNV32 SNV33 SNV34
HAR
g
Candidate causal variant effect
RMSE = 0.78
RMSE = 0.96
RMSE = 0.17
RMSE = 0.75
iPSC H3K4me3
K562 ZNF639
Log2(Human/Chimp)
Log2(Human/Human w/SNV1)
Log2(Human/Human w/SNV20)
Log2(Human/Human w/SNV21)
Log2(Human/Human w/SNV34)

502 **Figure 5: Motor neuron-specific chimpanzee-biased ASE for *GAD1* and ASCA for a HAR near the *GAD1***
503 **TSS. a)** Allelic ATAC-seq tracks are shown for the peak near the *GAD1* TSS that contains a HAR
504 (highlighted in yellow). **b)** The top panel shows allelic CPM of the CRE near the *GAD1* TSS across cell
505 types and the bottom panel shows the log fold-change across cell types. **c)** The top panel shows allelic
506 CPM of the *GAD1* gene across cell types and the bottom panel shows the log fold-change across cell
507 types. **d)** Outline of the process for variant effect prediction with Sei for *GAD1*. All input sequences to Sei
508 were centered at the HAR. The human sequence, the chimpanzee sequence, and modified sequences
509 with the human sequence altered at each substitution to match the chimpanzee sequence were fed into
510 the Sei sequence model to predict the effects of these variants on the chromatin state. **e)** Histogram of
511 the probabilities of various chromatin states and transcription factor binding predicted by Sei was
512 plotted for the human sequence, the chimpanzee sequence, and two examples in which the human
513 sequence with only one SNV "chimpanized" (human w/SNV) was input to Sei. The histogram of the
514 probability of the sequence having a particular epigenomic annotation (predicted by Sei) was plotted for
515 human, chimpanzee, human w/SNV1 changed to match the chimpanzee sequence, and human w/SNV21
516 changed to match the chimpanzee sequence. Two epigenomic annotations were labeled as examples
517 that show the different values output by Sei with these two different sequence inputs. **f)** Plot of the
518 predicted effects of all single nucleotide differences between human and chimpanzee in the Sei input
519 window centered at the HAR (highlighted in yellow). Positions were switched to the chimpanzee allele
520 individually. **g)** Scatterplots showing the correlation of the effects of four SNVs on Sei predictions with
521 the difference in Sei predictions between the human and chimpanzee sequences. The root mean square
522 error (RMSE) was computed and shown in each figure.

524 **Methods:**

525 **Generation of multiple human-chimpanzee hybrid cell types**

526 We used two previously described human-chimpanzee hybrid iPS cell lines (hybrid1 and hybrid2,
527 previously denoted Hy1-25 and Hy1-30 respectively) (Agoglia et al., 2021). Before differentiation, cells
528 were routinely cultured on matrigel in mTeSR1 or mTeSR Plus (Stem Cell Technologies cat #85850 or cat
529 #100-0276). Culture and *in vitro* differentiation of iPS cells into six cell types (motor neurons (MN),
530 cardiomyocytes (CM), hepatocyte progenitors (HP), pancreatic progenitors (PP), skeletal myocytes
531 (SKM), and retinal pigment epithelium (RPE)) was carried out by the Columbia Stem Cell Core Facility
532 using published protocols (Burridge et al., 2014; Chal et al., 2016; Korytnikov & Nostro, 2016; Mallanna
533 & Duncan, 2013; Maury et al., 2015; Sharma et al., 2019).

534

535 **Preparation of RNA-seq libraries**

536 All samples were cryopreserved in liquid nitrogen before RNA extraction (Milani et al., 2016). Cells were
537 gently thawed and then washed with PBS and cell pellets were collected via centrifugation at 1,000 RPM
538 for 5 minutes. Cell pellets were loosened by flicking the tube and an appropriate volume of Buffer RLT
539 based on the cell count were added following the RNeasy Mini Kit (Qiagen, 74104) protocol. Total RNA
540 extraction and on-column DNAse digestion were performed using RNeasy Mini Kit (Qiagen, 74104) and
541 RNase-Free DNase Set (Qiagen, 79254). RNA quality was assessed using the Agilent Bioanalyzer RNA Pico
542 assay. Only samples with an RNA integrity number (RIN) greater than or equal to 7 were used to prepare
543 cDNA libraries. All RNA-seq libraries except 3 motor neuron libraries (2 hybrid2 and 1 hybrid1) were
544 prepared using the TruSeq Stranded mRNA kit (Illumina, 20020594) and the TruSeq RNA CD Index Plate
545 (Illumina, 20019792) from between 100 ng and 1 ug total RNA following the manufacturer's protocols.
546 The other three motor neuron libraries were prepared using Illumina Stranded mRNA Prep (Illumina,
547 20040532) and IDT for Illumina RNA UD Indexes Set A, Ligation (Illumina, 20040553) due to low yield of

548 total RNA. Notably, the four motor neuron libraries did not cluster by library preparation method. All
549 libraries were normalized, pooled at an equimolar ratio using Qubit measurements, and sequenced on
550 an Illumina HiSeq 4000 to generate 2x150bp paired-end reads.
551
552 **Identification of confident human-chimpanzee SNVs**
553 To identify a confident list of human-chimpanzee SNVs that could be used to quantify allele-specific
554 expression and chromatin accessibility, we first downloaded hg38-panTro6 MAF files from UCSC and
555 whole-genome sequencing data generated from the parental human and chimpanzee iPS cells (in the
556 form of bam files aligned to hg38 and panTro5, generously provided by the Gilad lab). We first
557 converted them back to fastq files and then mapped reads to panTro6 and hg38 (we mapped both
558 human and chimpanzee to both reference genomes) using bowtie2 with the flags —very-sensitive-local -
559 p 16 (Langmead & Salzberg, 2012). We then used a modified version of our previous approach to filter
560 out SNVs that could not be confidently identified as homozygous in the human and chimpanzee parental
561 lines (Agoglia et al., 2021). Briefly, we extracted SNVs and indels from both human and chimpanzee MAF
562 files, counted reads in the WGS data that supported the human, chimpanzee, or an alternative base at
563 that position, then filtered out any SNVs with < 2 reads or < 90% of reads supporting that species' base.
564 We then reformatted files, merged with indels for use in Hornet, and generated a modified bed file of
565 SNVs that includes the human and chimpanzee base at the SNV position (van de Geijn et al., 2015).
566
567 **Generation of allele-specific count tables**
568 An allele specific expression mapping and calling pipeline adapted from Agoglia et al. and our updated
569 high-confidence SNV list was used. The whole pipeline was carried out twice independently using hg38
570 or panTro6 as the reference genome. This approach was taken to eliminate genes showing strong
571 mapping bias, defined here as genes with an absolute difference in log fold-change between the

572 panTro6 referenced and hg38 referenced runs greater than one. All sequencing reads were trimmed
573 with SeqPrep (adapters specified by the manufacturer for the different library preparation kits) and
574 mapped using STAR with two passes and the following parameters: --outFilterMultimapNmax 1 (Dobin
575 et al., 2013; John St. John, n.d.). Uniquely aligned reads were deduplicated with Picard and Hornet (an
576 implementation of WASP which first removes reads overlapping indels) was used to correct for mapping
577 bias (Broad Institute, n.d.; van de Geijn et al., 2015). Reads were assigned to either the human allele if
578 they contained one or more human-chimpanzee single nucleotide differences that matched the human
579 sequence and zero positions that matched the chimpanzee sequence (and vice versa for assigning reads
580 to the chimpanzee allele) and counted per gene as previously described (Agoglia et al., 2021).
581
582 **Detection of aneuploidy on chromosome 20 and slight chimpanzee parental contamination in PP**
583 **hybrid2 samples**
584 In our quality control process, we plotted the log fold-change for each gene along every chromosome
585 and inspected the results. This revealed a clear bias toward the human allele on a part of chromosome
586 20 for hybrid2 samples, suggesting chromosome 20 aneuploidy which was also reported by Agoglia et al
587 (Agoglia et al., 2021). As a result, we excluded chromosome 20 from all downstream analyses. In
588 addition, we found that PP hybrid2 samples had a slight bias toward the chimpanzee allele across every
589 chromosome which was most likely due to a small fraction of contaminating chimpanzee cells in these
590 samples. Rather than removing these samples, we normalized the allele-specific count tables by
591 subtracting a small number of reads from the chimpanzee allele counts calculated based on the biased
592 ratio summarized from genome wide human and chimpanzee allele counts, to force a global log fold-
593 change (across all autosomes except chromosome 20) of zero between the human and chimpanzee
594 alleles. We applied this normalization to all other samples as well. To evaluate the success of this
595 strategy, we took hybrid and chimpanzee parental iPSC RNA-seq from Agoglia et al (Agoglia et al., 2021)

596 from the same iPS cell lines as used in this study, and then simulated chimpanzee parental
597 contamination by mixing chimpanzee parental data into hybrid 2 data to reach similar a similar degree
598 of chimpanzee bias level to that observed in the PP hybrid2 samples. We then identified genes showing
599 ASE (see "Identifying genes with ASE") using the counts from the original hybrid samples, simulated
600 contaminated samples, and corrected simulated contaminated samples respectively and compared the
601 outputs (Supp Fig. 4).
602
603 **PCA and hierarchical clustering**
604 Allelic counts were normalized by DESeq2 rlog and principal components analysis (PCA) was performed
605 on rlog normalized allelic counts with default centering and scaling (Love et al., 2014). The top 1,000
606 variable genes with the highest variance of normalized allelic counts across all cell types were used to
607 compute Euclidean distance matrices. The R package pheatmap was used to do hierarchical clustering
608 and heatmap plotting.
609
610 **Identifying genes with ASE**
611 DESeq2 was used to measure allele-specific expression (ASE) in each cell type (Love et al., 2014). All
612 reads from chromosome 20 were removed (as mentioned above). Two replicates per hybrid line per cell
613 type (plus one additional replicate for SKM hybrid2 for a total of 3 samples) were used by DEseq2 with
614 model ~hybLine+Species to measure differential expression level. A likelihood ratio test (test="LRT",
615 betaPrior=FALSE) was used to compute p-values. P-values were then false discovery rate adjusted using
616 an implementation of the Benjamini-Hochberg correction in the R package qvalue (Benjamini &
617 Hochberg, 1995; Storey Lab, n.d.). Log fold-changes were shrunk as recommended by the DESeq2
618 pipeline (Zhu et al., 2019). Differentially expressed genes were defined as those with FDR < 0.05 when

619 aligned to hg38 and panTro6 as well as an absolute difference in log fold-change <= 1 when comparing
620 the results from the two alignments.
621
622 **Identifying cell type-specifically expressed genes**
623 For the more traditional definition of cell type-specific genes, we required transcripts per million (TPM)
624 < 1 for a gene in every cell type except one. In the cell type with TPM > 1, we varied how highly
625 expressed the gene had to be in that cell type (again using a TPM cutoff, varying between one and five)
626 to consider that gene to be specific to that cell type. A similar process to the one described in
627 "Identifying differentially expressed genes" was used to identify cell type-specific genes based on the
628 broader definition described in the main text. Rather than using allelic counts, total counts for each
629 sample (i.e. all uniquely mapping deduplicated reads regardless of their allelic origin) were computed by
630 summing all allelic and non-allelic counts**.** These counts were inputted to DESeq2 and the expression of
631 each gene was compared pairwise between all cell types (Love et al., 2014). Genes were defined as cell
632 type-specifically expressed in a cell type only if all pairwise comparisons between that cell type and
633 other cell types resulted in an FDR < 0.05 using both hg38 and panTro6 aligned counts. Due to the
634 markedly lower number of differentially expressed genes identified in SKM, results were computed both
635 including and excluding SKM. An analogous procedure was used to identify more broadly defined cell
636 type-specific peaks in the down-sampled ATAC-seq dataset. Peaks were defined as specific to a cell type
637 if the absolute log fold-change was greater than 0.5 across all pairwise comparisons with the other cell
638 types. We also tested an absolute log fold-change threshold of 1 to ensure that our results were not
639 sensitive to the choice of cutoff.
640
641 **Enrichment test for genes with cell type-specific expression patterns and genes showing ASE**

642 Odds ratios were calculated using the unconditional maximum likelihood estimate implemented in the R
643 package epitools function oddsratio.wald (), and 95% confidence intervals and p-values were calculated
644 using the normal approximation. A directly analogous procedure was performed to test for enrichment
645 of peaks with ASCA and cell type-specific peaks.
646
647 **Enrichment test stratified by expression level or evolutionary constraint**
648 Enrichment tests were carried out as in 'Enrichment test of cell type-specific expression patterns and
649 genes showing ASE' except that genes were split into five equal size bins depending on which factors
650 were used to stratify genes, and tests were done in each bin. When stratifying by expression level, genes
651 were ordered in ascending order based on expression level (TPM) and then split into 5 equal size bins
652 where genes in the 0-20% bin are the most lowly expressed genes and genes in the 80-100% bin are the
653 most highly expressed genes. When stratifying by constraint metrics such as ASE variance or pHI, genes
654 were ordered in ascending order based on ASE variance values and then split into five equal size bins
655 where the 0-20% bin contains genes with the lowest ASE variance (i.e. most evolutionarily constrained)
656 and the 80-100% bin contains genes with highest ASE variance (i.e. least evolutionarily constrained). To
657 stratify the ATAC data by constraint, we used the "QCed genomic constraint by 1kb regions" computed
658 by the gnomAD consortium (S. Chen et al., 2022). We further removed any regions that overlapped
659 protein coding exons from the human gtf file using bedtools subtract (Quinlan & Hall, 2010). If a peak
660 overlapped two or more 1 kilobase windows, it was assigned to the window with the highest constraint,
661 mirroring the procedure used by the gnomAD consortium to assign peaks to ENCODE regulatory
662 elements (S. Chen et al., 2022). Once the peaks were ranked by this metric, a procedure identical to that
663 for the gene expression constraint metrics outlined above was performed.
664
665 **Identification of lineage-specific selection on gene expression**

666 We used a modified version of our previously published pipeline, which uses ASE values from many
667 individuals of a single species to estimate cis-regulatory constraint of each gene (Starr et al., 2023). We
668 restricted these ASE values to GTEx samples from the tissue (s) of origin for each cell type (with the
669 exceptions of RPE which was compared to all GTEx samples and MN which was compared to all brain
670 and peripheral nerve samples as more closely matches tissues such as eyes for RPE are not available in
671 GTEx). We then used the Mann-Whitney U test to compare the human population ASE distribution to
672 the human-chimpanzee ASE distribution as previously described (Starr et al., 2023). We then used the
673 previously described signed ranking by Mann-Whitney p-value that incorporates whether a gene has
674 human or chimpanzee-biased ASE with GSEAPY and the binomial test to identify instances of lineage-
675 specific selection (Starr et al., 2023). Due to the focus on tissue-specificity, we did not filter redundant
676 gene sets with GSEAPY FDR < 0.25 in multiple cell types (Starr et al., 2023; Subramanian et al., 2005).
677

678 **Preparation of ATAC-seq libraries**

679 We used the OmniATAC protocol with the only modification being the use of 25,000 cells instead of
680 50,000 since the fused iPS cells are tetraploid (Corces et al., 2017). All samples for ATAC-seq prep were
681 from the same vials used in RNA-seq library preparation except for the motor neuron libraries due to the
682 low yield of total RNA extracted from motor neurons. After library preparation and running samples on a
683 Bioanalyzer, we noticed a considerable number of fragments greater than 1000 bases in length. To
684 reduce these fragments, we size selected with Ampure beads using the protocol from the Kaestner lab
685 available here: https://www.med.upenn.edu/kaestnerlab/assets/user-content/documents/ATAC-
686 seq-Protocol- (Omni)-Kaestner-Lab.pdf.
687 After size selection and rerunning on the Bioanalzyer, we pooled the libraries together and sequenced
688 them to compute quality control metrics. We used the R package ChrAccR to compute TSS enrichment
689 scores (Mueller, Fabian, n.d.). We pooled all libraries with TSS enrichment score greater than 3.5. This

690 resulted in 2 CM libraries, 2 MN libraries, 2 PP libraries, 1 SKM library, and 1 HP library. After pooling,
691 libraries were sequenced on an Illumina Hiseq 4000 to produce 2x150 paired-end reads.
692
693 **Mapping the ATAC-seq data**
694 We trimmed reads using SeqPrep and then mapped them to the hg38 and panTro6 reference genomes
695 with bowtie2 in paired-end mode (John St. John, n.d.; Langmead & Salzberg, 2012). The following
696 parameters were used: -X 2000 --very-sensitive-local -p 16. After mapping, duplicates were removed via
697 Picard MarkDuplicates (Broad Institute, n.d.). We then removed multi-mapping reads with the command
698 samtools view -b -q 10 (Li et al., 2009). Due to the format of bowtie2's output, running Hornet on all
699 reads at once was excessively RAM intensive. Therefore, we split the bam files by chromosome and ran
700 Hornet on each of the chromosomes separately. We used the files of SNVs and indels generated as
701 described above as input to Hornet. After Hornet finished running, we used samtools merge to merge all
702 autosomes and sex chromosomes (we excluded the mitochondrial genome) to create a final bam file for
703 downstream analysis (Li et al., 2009).
704
705 **Peak calling and filtering**
706 As only one replicate was available for SKM and HP, we generated two pseudo-replicates by randomly
707 assigning reads to one of two files using Picard SplitSamByNumberOfReads (Broad Institute, n.d.). We
708 then called peaks on each file separately, as well as a merged file containing all the reads from a
709 particular cell type. For example, for MN, both replicates were pooled and peaks were called on that file
710 as well as the two replicates separately. Before peak calling, all bam files were converted to bed files.
711 We called peaks using MACS2 callpeak with the following arguments: -f BED -p 0.01 --nomodel --shift 75
712 --extsize 150 -B --SPMR --keep-dup all --call-summits (Y. Zhang et al., 2008, p. 2). We called peaks on
713 both the chimpanzee-referenced and human-referenced bam files. After peak calling, we sought to filter

714 peaks using a modified version of the ENCODE pipeline designed to eliminate peaks that lack a one-to-
715 one ortholog between humans and chimpanzees. The following pipeline was run on each cell type
716 separately. We first filtered peaks that were not called in both replicates as well as the pooled file using
717 code from the ENCODE pipeline based on bedtools and awk (Quinlan & Hall, 2010). We then used a
718 custom Python script to merge overlapping peaks and used UCSC LiftOver to lift the peaks from hg38 to
719 the panTro6 and back to hg38 as well as from panTro6 to hg38 (Kuhn et al., 2013). We then used
720 bedtools to intersect the resulting human referenced files and filtered out any peaks that did not have at
721 least 25% overlap with a peak in the other file (Quinlan & Hall, 2010). After filtering out peaks
722 overlapping ENCODE blacklisted regions and merging overlapping peaks again, we lifted the file that was
723 originally chimpanzee-referenced back to the chimpanzee genome (Amemiya et al., 2019). Finally, we
724 removed human-referenced peaks if their chimpanzee-referenced counterpart failed to LiftOver (Kuhn
725 et al., 2013).
726
727 **Annotating the peak lists**
728 To annotate the peaks, we used the list of TSS defined by Horlbeck et al. to annotate peaks (Horlbeck et
729 al., 2016). We lifted over each TSS to hg38, expanded 1000 bases on either side of the midpoint of each
730 TSS to generate promoters, and merged any promoters that overlapped while retaining all unique gene
731 names associated with the promoter (Kuhn et al., 2013). We then used reciprocal LiftOver with panTro6
732 to filter out non-orthologous promoters and used bedtools intersect to link peaks to promoters and
733 expanded the peak to include the entirety of the promoter if necessary (Quinlan & Hall, 2010). Through
734 this process, we also outputted a list of non-promoter CREs (sometimes labeled as enhancers as
735 enhancers are thought to be the most common type of CRE). We took this list and used bedtools closest
736 to link them to the two closest protein coding genes (Quinlan & Hall, 2010). Notably, the gene naming
737 conventions differ for the Horlbeck et al. TSS list and the GTF file used for RNA-seq processing. We

738 altered all gene names in peaks to match those found in the GTF file. In some cases, the gene no longer
739 existed in the updated hg38 GTF in which case the gene name was replaced with NAN.
740
741 **Generating a unified peak list**
742 We next merged our cell type-specific peak list across all five cell types to create a unified peak list. To
743 do this, we iteratively intersected all the peaks with bedtools and then merged any overlapping peaks
744 (Quinlan & Hall, 2010). Finally, we added back any peaks that did not intersect a peak found in any other
745 cell types. We then took the chimpanzee and human-referenced versions of these peak lists and ran
746 them through the LiftOver-based non-homologous peak filtering pipeline described above to generate a
747 final file of all identified peaks as well as which cell type (s) they were called in (Kuhn et al., 2013). Then,
748 we reran the annotation pipeline described in 'Annotating the peak lists' on this new set of peaks.
749
750 **Counting reads in peaks and further peak filtering**
751 First, we split the bam files into reads that we could confidently assign to the chimpanzee genome and
752 reads we could assign to the human genome. We used our bed file of high-confidence SNVs and
753 required at least one SNV matching the human genome as well as no SNVs matching the chimpanzee
754 genome for a read to be assigned to human (and vice versa for chimp). We then used a custom Python
755 script to reformat the peak list bed files as GTF files and used HTSeq to count reads in peaks using the
756 following parameters: -s no -m union -r pos (Anders et al., 2015). We only kept peaks if they had a mean
757 read count across replicates within a cell type of at least 25 from either allele. For example, if a peak has
758 an average of 27 reads from the human allele and an average of 10 reads from the chimpanzee allele in
759 MN, that peak would be kept in MN. On the other hand, if the same peak had an average of 24 reads
760 from the human allele and an average of 10 reads from the chimpanzee allele in CM, that peak would be
761 discarded for CM.

762

763 We next filtered the reads to remove peaks that might be differentially accessible but show evidence of
764 mapping bias or do not agree between replicates. To do this, we removed any peaks with an absolute
765 log fold-change greater than one in one replicate but with a fold-change of any magnitude in the
766 opposite direction in the other. This was not done for SKM or HP as we had only one replicate. We then
767 removed any peaks that had a log fold-change in opposite directions with an absolute difference greater
768 than 1 in at least one replicate when comparing the human-referenced and chimpanzee-referenced
769 counts. Finally, as described in section ‘‘Detection of aneuploidy on chromosome 20 and slight
770 chimpanzee parental contamination in PP hybrid2 samples’ for RNA-seq data analysis, we removed any
771 peaks on chr20 and took this as our final list of peaks for downstream analyses. Allelic counts were
772 normalized as described in the RNA-seq data analysis. We tested for allele-specific chromatin
773 accessibility (ASCA) using the binomial test applied to the normalized allelic counts (summed by species
774 within a cell type). We considered any peaks with a binomial p-value less than 0.05 to be nominally
775 differentially accessible.

776

777 **Down-sampling to identify cell type-specific ATAC-seq peaks**

778 As the number of peaks detected by ATAC-seq is generally a function of read depth and our read depth
779 varied widely across cell types, we restricted to one replicate (always hybrid1 if two replicates were
780 available) and down-sampled reads to match the SKM sample with lowest sequencing depth. We then
781 called peaks for cell types with a single ATAC replicate as described above.

782

783 **Allelic chromatin accessibility tracks**

784 Allelic bam files with reads originating from the human allele and the chimpanzee allele (respectively)
785 were obtained as described in ‘Counting reads in peaks and further peak filtering’. Two replicates in CM,

786 MN, and PP were pooled by cell type. Bam files were converted into bigWig files using python package
787 deepTools bamCoverage with options: --binSize 1 --normalizeUsing CPM --effectiveGenomeSize
788 2862010578 --ignoreForNormalization chr20 --extendReads (Ramírez et al., 2014). Tracks were
789 visualized and plotted using the python package pyGenomeTracks (Lopez-Delisle et al., 2021). When
790 comparing human and chimpanzee log fold-change track differences in each cell type, deepTools
791 bigwigCompare was used to compare between human bigWig and chimpanzee bigWig with options: --
792 pseudocount 1 --skipZeroOverZero --operation log2 -bs 1 (Ramírez et al., 2014).
793
794 **ChromHMM annotation and correlation with ASE**
795 A universal chromHMM annotation was obtained for each peak based on overlap with any of the 15
796 categories in chromHMM (excluding the blacklist category, for which peaks had already been removed)
797 (Ernst & Kellis, 2017; Vu & Ernst, 2022). Divergence was measured as the z-score transformed median of
798 the absolute log fold-change of human and chimpanzee normalized counts in each peak. Each peak was
799 assigned to the closest gene and then Pearson correlation was computed between the chromatin
800 accessibility log fold-change and the expression log fold-change for each peak and its nearest gene.
801 Pearson correlation was computed only on categories including at least 15 peaks. When showing results
802 for differentially accessible peaks, only peaks with binomial p-values less than 0.05 were kept and used
803 in computing the Pearson correlation. When assigning a unique chromHMM to each peak, the
804 chromHMM category that covered the largest portion of each peak was used. When filtering out
805 promoter-related annotations, peaks covering any promoter-related chromHMM categories (“TSS”,
806 “flanking promoter” and “bivalent promoter”) were filtered out and the analysis described above was
807 repeated.
808

809 **Computation of differential expression enrichment (dEE) and differential chromatin accessibility**
810 **enrichment (dCAE)**
811 For each target cell type, taking CM as an example, the log fold-change for gene A was fixed as target log
812 fold-change, and the log fold-changes for gene A in the remaining cell types with an opposing sign
813 (compared to the target log fold-change) were set to zero. Then, the dEE value was calculated as the
814 proportion of the target log fold-change in the sum of the zeroed log fold-changes across all cell types.
815 For example, the dEE for gene A in CM would be abs (target LFC)/sum (abs (LFC after zeroing))). dEE
816 ranges from zero to one and low dEE value indicates differential expression with similar magnitude and
817 direction across cell types, and/or the gene does not have any strong allelic bias, whereas a high dEE
818 value indicates that this gene is only strongly differentially expressed (with the sign the log fold-change
819 has in that cell type) in a particular cell type. dCAE uses the same procedure as dEE except the table is
820 populated with the log fold-changes derived from chromatin accessibility measurements. dEE and dCAE
821 are sensitive to the inclusion or exclusion of cell types (by definition), so we excluded RPE when
822 integrative analysis combining results from dEE and dCAE was performed (to match the cell types for
823 which dCAE could be computed, Supp Fig. 25b). After restricting to genes defined as having significant
824 ASE or significant ASCA, we defined genes with dEE >= 0.75 in a particular cell type as showing cell type-
825 specific ASE and peaks with dCAE >= 0.75 in one cell type as showing cell type-specific ASCA. We used
826 bedtools intersect to intersect the peaks with our list of human-chimpanzee single nucleotide
827 differences and the 241-way placental mammal PhyloP scores (Quinlan & Hall, 2010; Sullivan et al.,
828 2023). We also checked whether peaks that contained human-chimpanzee differences in sites with high
829 PhyloP scores were in the list of HARs described in Girskis et al (Girskis et al., 2021).
830
831 **Predicting regulatory activity with single-variant resolution**

832 We used sequences in fasta format as input to the deep neural network model Sei (K. M. Chen et al.,
833 2022). Sei requires a 4096 base pair input sequence, so we put the center of our region of interest at the
834 center of the input window and expanded equally on either side to contain 4096 base pairs. The human
835 sequence was retrieved from hg38 and the corresponding chimpanzee sequence was retrieved from
836 panTro6. The effect size when comparing the probabilities of each sequence having a particular
837 chromatin state was computed as the log of the human sequence probability divided by the chimpanzee
838 sequence probability. Only annotations for which either the chimpanzee sequence or the human
839 sequence had a probability value greater than or equal to 0.5 were kept for downstream analysis. All
840 SNVs between human and chimpanzee in this input window were identified and ordered based on
841 coordinates. For each SNV position, the human sequence was changed to the chimpanzee allele at that
842 position to generate a new sequence that was input to Sei. The log fold-change for each chromatin
843 annotation was computed for each input sequence as described above and used as a measure of the
844 effect of this change on the sequence. Similarly, an indel can be introduced to modify the human
845 sequence and input to Sei. With indels, the center of the regions of interest (promoter or HAR) were
846 always at the center of the input window and the start or end of the sequence inputted to Sei could
847 possibly lose or gain base pairs. However, we found that for the small indels shown here this had
848 essentially no effect on the Sei output.
849

850 **Processing of publicly available datasets**

851 The data from Blake et al. and Pavlovic et al. were processed as previously described (Blake et al., 2020;
852 Pavlovic et al., 2018; Starr et al., 2023). For the Pavlovic et al. data, log fold-changes were computed in
853 DESeq2 with the scaled proportion of cardiomyocytes present in each sample (available in the
854 supplemental materials of Pavlovic et al.), sex, and whether cardiomyocytes were treated with T3 as
855 covariates (i.e. using the model ~sex+scaled_proportion_cardiomyocytes+T3_Treatment+species)

856 (Pavlovic et al., 2018). No covariates were included for Blake et al. as they had little impact on the data
857 (Blake et al., 2020). The log fold-changes and FDR corrected p-values were directly downloaded from the
858 supplemental materials of Kozlenkov et al. (Kozlenkov et al., 2020).
859
860 The processed data from Ma et al. (Ma et al., 2022) were downloaded from
861 http://resources.sestanlab.org/PFC/. We pseudobulked the data by cell type by summing counts within
862 each individual. We then separately input each pairwise comparison of two species (human to
863 chimpanzee or human to rhesus macaque) into DESeq2 with no covariates to test for differential
864 expression and compute log fold-changes.
865
866 The counts tables from Kanton et al.[12] were downloaded from
867 https://www.ebi.ac.uk/biostudies/arrayexpress/studies/E-MTAB-7552 and processed with SCANPY
868 (Kanton et al., 2019, p. 29409532; Wolf et al., 2018). The data were filtered by removing cells with
869 n_genes_by_counts > 2500 and >5% mitochondrial reads. We also removed cells with fewer than 200
870 unique genes and genes that had non-zero counts in fewer than 3 cells. After filtering, any chimpanzee
871 cells not falling in the category (defined by Kanton et al. (Kanton et al., 2019)) “ventral forebrain
872 progenitors and neurons” were eliminated and human cells not in the categories "ventral progenitors
873 and neurons 1", "ventral progenitors and neurons 2", or "ventral progenitors and neurons 3" were
874 similarly eliminated. We then merged the two counts tables, normalized/logarithmized the counts,
875 computed PCA, used harmony to integrate cells from different species (human and chimpanzee), and
876 found nearest neighbors with the harmonized principal components (Korsunsky et al., 2019). We then
877 ran Leiden clustering with resolution = 0.5 to identify 7 subclusters (one of which appeared to be a
878 technical artifact with very low counts that was removed) (Traag et al., 2019).

We identified cell types and lineages using canonical marker genes (*MKI67* and *HES5* for progenitors, *NKX2-1* and *LHX6* for the medial ganglionic eminence or MGE, *MEIS2* and *ZFHX3* for the lateral ganglionic eminence or LGE, and *SCGN* and *NR2F1* for the caudal ganglionic eminence or CGE) (Su-Feher et al., 2022). We then used the implementation of PAGA in SCANPY to compute pseudotime using the first cell in the progenitor subcluster as the root (Wolf et al., 2019). We binned cells into five equal bins along pseudotime and compared the expression of cells with non-zero counts for *GAD1* in each pseudotime bin. Within each bin, we used a Wilcoxon test to test for higher expression of *GAD1* in chimpanzee cells compared to human cells. We repeated the pseudotime analysis, binning, and comparing of *GAD1* gene expression for each subtrajectory (MGE, LGE, and CGE).

Description of Additional file 1: This file contains an extended evaluation of the success of the differentiations in generating the desired cell type and other cell types likely to be present in each sample.

Description of Additional file 2: This file contains the results of running the test for selection described by Starr et al on each cell type.

Description of Additional file 3: This file contains the peak-gene pairs that had concordant high dCAE and high dEE in each cell type.

Declarations: The authors have nothing to declare.

Ethics approval and consent to participate: Not relevant to our study.

903

904 **Consent for publication:** Not relevant to our study.

905

906 **Availability of data and materials:** Raw and processed data generated by this study are publicly
907 available through the Gene Expression Omnibus under accession GSE232949:
908 https://www.ncbi.nlm.nih.gov/geo/query/acc.cgi?acc=GSE232949. The snRNAseq data from Ma et al.
909 are available here: http://resources.sestanlab.org/PFC/. The scRNAseq data from Kanton et al. are
910 available here: https://www.ebi.ac.uk/biostudies/arrayexpress/studies/E-MTAB-7552. The bulk RNA-seq
911 data from Blake et al. and Pavlovic et al. are available here:
912 https://www.ncbi.nlm.nih.gov/geo/query/acc.cgi?acc=GSE112356 and here:
913 https://www.ncbi.nlm.nih.gov/geo/query/acc.cgi?acc=GSE110471 respectively. The log fold-changes
914 and associated statistics were used directly from the supplemental materials of Kozlenkov et al. The
915 human-chimp pairwise alignment used to identify SNVs and indels is available here:
916 https://hgdownload.soe.ucsc.edu/goldenPath/hg38/vsPanTro6/. The human and chimpanzee genomes
917 used are available here: https://hgdownload.soe.ucsc.edu/goldenPath/hg38/bigZips/ and here:
918 https://hgdownload.soe.ucsc.edu/goldenPath/panTro6/bigZips/ respectively. The 241-way PhyloP
919 scores were downloaded from here:
920 https://hgdownload.soe.ucsc.edu/goldenPath/hg38/cactus241way/. The "QCed genomic constraint by
921 1kb regions" from the gnomAD consortium are available here:
922 https://gnomad.broadinstitute.org/downloads#v3. All scripts for performing analyses and making
923 figures in this manuscript is publicly available at https://github.com/banwang27/multi-celltypes.

924

925 **Competing interests:** The authors have no competing interests to declare.

926

Funding: Funding for this work came from NIH R01HG012285. A.L.S was supported by an NDSEG fellowship.

Author contributions: HBF conceived of the study. ALS and BW performed all analysis, visualization, validation, and writing of software. ALS wrote the manuscript with input from BW and HBF. BW made all figures with input from ALS and HBF. All authors approved the publication of the manuscript.

Acknowledgements: The authors wish to acknowledge the by the Columbia Stem Cell Core for their hard work in differentiating these cells. We also acknowledge members of the Fraser lab past and present for helpful discussion. BioRender was used to generate Figures 1a, 2a, and 3a.

938 Agoglia, R. M., Sun, D., Birey, F., Yoon, S.-J., Miura, Y., Sabatini, K., Pașca, S. P., & Fraser, H.
939 B. (2021). Primate cell fusion disentangles gene regulatory divergence in
940 neurodevelopment. *Nature*, *592* (7854), 421–427. https://doi.org/10.1038/s41586-021-
941 03343-3
942 Akbar, M., Calderon, F., Wen, Z., & Kim, H.-Y. (2005). Docosahexaenoic acid: A positive
943 modulator of Akt signaling in neuronal survival. *Proceedings of the National Academy of*
944 *Sciences*, *102* (31), 10858–10863. https://doi.org/10.1073/pnas.0502903102
945 Amemiya, H. M., Kundaje, A., & Boyle, A. P. (2019). The ENCODE Blacklist: Identification of
946 Problematic Regions of the Genome. *Scientific Reports*, *9* (1), 9354.
947 https://doi.org/10.1038/s41598-019-45839-z
948 Anders, S., Pyl, P. T., & Huber, W. (2015). HTSeq—A Python framework to work with high-
949 throughput sequencing data. *Bioinformatics (Oxford, England)*, *31* (2), 166–169.
950 https://doi.org/10.1093/bioinformatics/btu638
951 Arai, Y., Funatsu, N., Numayama-Tsuruta, K., Nomura, T., Nakamura, S., & Osumi, N. (2005).
952 Role of Fabp7, a downstream gene of Pax6, in the maintenance of neuroepithelial cells
953 during early embryonic development of the rat cortex. *The Journal of Neuroscience: The*
954 *Official Journal of the Society for Neuroscience*, *25* (42), 9752–9761.
955 https://doi.org/10.1523/JNEUROSCI.2512-05.2005
956 Ben-Ari, Y., Khalilov, I., Kahle, K. T., & Cherubini, E. (2012). The GABA Excitatory/Inhibitory
957 Shift in Brain Maturation and Neurological Disorders. *The Neuroscientist*, *18* (5), 467–
958 486. https://doi.org/10.1177/1073858412438697
959 Benito-Kwiecinski, S., Giandomenico, S. L., Sutcliffe, M., Riis, E. S., Freire-Pritchett, P., Kelava,
960 I., Wunderlich, S., Martin, U., Wray, G. A., McDole, K., & Lancaster, M. A. (2021). An
961 early cell shape transition drives evolutionary expansion of the human forebrain. *Cell*,
962 *184* (8), 2084-2102.e19. https://doi.org/10.1016/j.cell.2021.02.050

Benjamini, Y., & Hochberg, Y. (1995). Controlling the False Discovery Rate: A Practical and Powerful Approach to Multiple Testing. *Journal of the Royal Statistical Society: Series B (Methodological)*, *57* (1), 289–300. https://doi.org/10.1111/j.2517-6161.1995.tb02031.x

Blake, L. E., Roux, J., Hernando-Herraez, I., Banovich, N. E., Perez, R. G., Hsiao, C. J., Eres, I., Cuevas, C., Marques-Bonet, T., & Gilad, Y. (2020). A comparison of gene expression and DNA methylation patterns across tissues and species. *Genome Research*, *30* (2), 250–262. https://doi.org/10.1101/gr.254904.119

Broad Institute. (n.d.). *Picard*.

Brose, N., Brunger, A., Cafiso, D., Chapman, E. R., Diao, J., Hughson, F. M., Jackson, M. B., Jahn, R., Lindau, M., Ma, C., Rizo, J., Shin, Y.-K., Söllner, T. H., Tamm, L., Yoon, T.-Y., & Zhang, Y. (2019). Synaptic vesicle fusion: Today and beyond. *Nature Structural & Molecular Biology*, *26* (8), 663–668. https://doi.org/10.1038/s41594-019-0277-z

Buenrostro, J. D., Giresi, P. G., Zaba, L. C., Chang, H. Y., & Greenleaf, W. J. (2013). Transposition of native chromatin for fast and sensitive epigenomic profiling of open chromatin, DNA-binding proteins and nucleosome position. *Nature Methods*, *10* (12), 1213–1218. https://doi.org/10.1038/nmeth.2688

Burridge, P. W., Matsa, E., Shukla, P., Lin, Z. C., Churko, J. M., Ebert, A. D., Lan, F., Diecke, S., Huber, B., Mordwinkin, N. M., Plews, J. R., Abilez, O. J., Cui, B., Gold, J. D., & Wu, J. C. (2014). Chemically defined generation of human cardiomyocytes. *Nature Methods*, *11* (8), 855–860. https://doi.org/10.1038/nmeth.2999

Calderari, S., Ria, M., Gérard, C., Nogueira, T. C., Villate, O., Collins, S. C., Neil, H., Gervasi, N., Hue, C., Suarez-Zamorano, N., Prado, C., Cnop, M., Bihoreau, M.-T., Kaisaki, P. J., Cazier, J.-B., Julier, C., Lathrop, M., Werner, M., Eizirik, D. L., & Gauguier, D. (2018). Molecular genetics of the transcription factor GLIS3 identifies its dual function in beta cells and neurons. *Genomics*, *110* (2), 98–111. https://doi.org/10.1016/j.ygeno.2017.09.001

Caporali, A., & Emanueli, C. (2009). Cardiovascular actions of neurotrophins. *Physiological Reviews*, *89* (1), 279–308. https://doi.org/10.1152/physrev.00007.2008

Castel, S. E., Aguet, F., Mohammadi, P., GTEx Consortium, Aguet, F., Anand, S., Ardlie, K. G., Gabriel, S., Getz, G. A., Graubert, A., Hadley, K., Handsaker, R. E., Huang, K. H., Kashin, S., Li, X., MacArthur, D. G., Meier, S. R., Nedzel, J. L., Nguyen, D. T., … Lappalainen, T. (2020). A vast resource of allelic expression data spanning human tissues. *Genome Biology*, *21* (1), 234. https://doi.org/10.1186/s13059-020-02122-z

Castro-Mondragon, J. A., Riudavets-Puig, R., Rauluseviciute, I., Lemma, R. B., Turchi, L., Blanc-Mathieu, R., Lucas, J., Boddie, P., Khan, A., Manosalva Pérez, N., Fornes, O., Leung, T. Y., Aguirre, A., Hammal, F., Schmelter, D., Baranasic, D., Ballester, B., Sandelin, A., Lenhard, B., … Mathelier, A. (2022). JASPAR 2022: The 9th release of the open-access database of transcription factor binding profiles. *Nucleic Acids Research*, *50* (D1), D165–D173. https://doi.org/10.1093/nar/gkab1113

Chal, J., Al Tanoury, Z., Hestin, M., Gobert, B., Aivio, S., Hick, A., Cherrier, T., Nesmith, A. P., Parker, K. K., & Pourquié, O. (2016). Generation of human muscle fibers and satellite-like cells from human pluripotent stem cells in vitro. *Nature Protocols*, *11* (10), 1833–1850. https://doi.org/10.1038/nprot.2016.110

Chen, K. M., Wong, A. K., Troyanskaya, O. G., & Zhou, J. (2022). A sequence-based global map of regulatory activity for deciphering human genetics. *Nature Genetics*, *54* (7), 940–949. https://doi.org/10.1038/s41588-022-01102-2

Chen, S., Francioli, L. C., Goodrich, J. K., Collins, R. L., Kanai, M., Wang, Q., Alföldi, J., Watts, N. A., Vittal, C., Gauthier, L. D., Poterba, T., Wilson, M. W., Tarasova, Y., Phu, W., Yohannes, M. T., Koenig, Z., Farjoun, Y., Banks, E., Donnelly, S., … Karczewski, K. J. (2022). *A genome-wide mutational constraint map quantified from variation in 76,156 human genomes* [Preprint]. Genetics. https://doi.org/10.1101/2022.03.20.485034

1014 Choi, W.-S., Xu, X., Goruk, S., Wang, Y., Patel, S., Chow, M., Field, C. J., & Godbout, R.
1015 (2021). FABP7 Facilitates Uptake of Docosahexaenoic Acid in Glioblastoma Neural
1016 Stem-like Cells. *Nutrients*, *13* (8), 2664. https://doi.org/10.3390/nu13082664
1017 Collins, R. L., Glessner, J. T., Porcu, E., Lepamets, M., Brandon, R., Lauricella, C., Han, L.,
1018 Morley, T., Niestroj, L.-M., Ulirsch, J., Everett, S., Howrigan, D. P., Boone, P. M., Fu, J.,
1019 Karczewski, K. J., Kellaris, G., Lowther, C., Lucente, D., Mohajeri, K., … Talkowski, M.
1020 E. (2022). A cross-disorder dosage sensitivity map of the human genome. *Cell*, *185* (16),
1021 3041-3055.e25. https://doi.org/10.1016/j.cell.2022.06.036
1022 Combs, P. A., Krupp, J. J., Khosla, N. M., Bua, D., Petrov, D. A., Levine, J. D., & Fraser, H. B.
1023 (2018). Tissue-Specific cis-Regulatory Divergence Implicates eloF in Inhibiting
1024 Interspecies Mating in Drosophila. *Current Biology*, *28* (24), 3969-3975.e3.
1025 https://doi.org/10.1016/j.cub.2018.10.036
1026 Conway, J. R., Lex, A., & Gehlenborg, N. (2017). UpSetR: An R package for the visualization of
1027 intersecting sets and their properties. *Bioinformatics*, *33* (18), 2938–2940.
1028 https://doi.org/10.1093/bioinformatics/btx364
1029 Corces, M. R., Trevino, A. E., Hamilton, E. G., Greenside, P. G., Sinnott-Armstrong, N. A.,
1030 Vesuna, S., Satpathy, A. T., Rubin, A. J., Montine, K. S., Wu, B., Kathiria, A., Cho, S.
1031 W., Mumbach, M. R., Carter, A. C., Kasowski, M., Orloff, L. A., Risca, V. I., Kundaje, A.,
1032 Khavari, P. A., … Chang, H. Y. (2017). An improved ATAC-seq protocol reduces
1033 background and enables interrogation of frozen tissues. *Nature Methods*, *14* (10), 959–
1034 962. https://doi.org/10.1038/nmeth.4396
1035 De Rosa, A., Pellegatta, S., Rossi, M., Tunici, P., Magnoni, L., Speranza, M. C., Malusa, F.,
1036 Miragliotta, V., Mori, E., Finocchiaro, G., & Bakker, A. (2012). A radial glia gene marker,
1037 fatty acid binding protein 7 (FABP7), is involved in proliferation and invasion of
1038 glioblastoma cells. *PloS One*, *7* (12), e52113.
1039 https://doi.org/10.1371/journal.pone.0052113

1040 Dobin, A., Davis, C. A., Schlesinger, F., Drenkow, J., Zaleski, C., Jha, S., Batut, P., Chaisson,
1041 M., & Gingeras, T. R. (2013). STAR: Ultrafast universal RNA-seq aligner. *Bioinformatics*
1042 *(Oxford, England)*, *29* (1), 15–21. https://doi.org/10.1093/bioinformatics/bts635
1043 Ebrahimi, M., Yamamoto, Y., Sharifi, K., Kida, H., Kagawa, Y., Yasumoto, Y., Islam, A.,
1044 Miyazaki, H., Shimamoto, C., Maekawa, M., Mitsushima, D., Yoshikawa, T., & Owada,
1045 Y. (2016). Astrocyte-expressed FABP7 regulates dendritic morphology and excitatory
1046 synaptic function of cortical neurons. *Glia*, *64* (1), 48–62.
1047 https://doi.org/10.1002/glia.22902
1048 Ernst, J., & Kellis, M. (2017). Chromatin-state discovery and genome annotation with
1049 ChromHMM. *Nature Protocols*, *12* (12), 2478–2492.
1050 https://doi.org/10.1038/nprot.2017.124
1051 Feldblum, S., Erlander, M. G., & Tobin, A. J. (1993). Different distributions of GAD65 and
1052 GAD67 mRNAS suggest that the two glutamate decarboxylases play distinctive
1053 functional roles. *Journal of Neuroscience Research*, *34* (6), 689–706.
1054 https://doi.org/10.1002/jnr.490340612
1055 Field, A. R., Jacobs, F. M. J., Fiddes, I. T., Phillips, A. P. R., Reyes-Ortiz, A. M., LaMontagne,
1056 E., Whitehead, L., Meng, V., Rosenkrantz, J. L., Olsen, M., Hauessler, M., Katzman, S.,
1057 Salama, S. R., & Haussler, D. (2019). Structurally Conserved Primate LncRNAs Are
1058 Transiently Expressed during Human Cortical Differentiation and Influence Cell-Type-
1059 Specific Genes. *Stem Cell Reports*, *12* (2), 245–257.
1060 https://doi.org/10.1016/j.stemcr.2018.12.006
1061 Fraser, H. B. (2011). Genome-wide approaches to the study of adaptive gene expression
1062 evolution: Systematic studies of evolutionary adaptations involving gene expression will
1063 allow many fundamental questions in evolutionary biology to be addressed. *BioEssays*,
1064 *33* (6), 469–477. https://doi.org/10.1002/bies.201000094

1065 Fraser, H. B. (2013). Gene expression drives local adaptation in humans. *Genome Research*,
1066 *23* (7), 1089–1096. https://doi.org/10.1101/gr.152710.112
1067 Fraser, H. B. (2019). Improving Estimates of Compensatory cis–trans Regulatory Divergence.
1068 *Trends in Genetics*, *35* (1), 3–5. https://doi.org/10.1016/j.tig.2018.09.003
1069 García-Pérez, R., Esteller-Cucala, P., Mas, G., Lobón, I., Di Carlo, V., Riera, M., Kuhlwilm, M.,
1070 Navarro, A., Blancher, A., Di Croce, L., Gómez-Skarmeta, J. L., Juan, D., & Marquès-
1071 Bonet, T. (2021). Epigenomic profiling of primate lymphoblastoid cell lines reveals the
1072 evolutionary patterns of epigenetic activities in gene regulatory architectures. *Nature*
1073 *Communications*, *12* (1), 3116. https://doi.org/10.1038/s41467-021-23397-1
1074 Girskis, K. M., Stergachis, A. B., DeGennaro, E. M., Doan, R. N., Qian, X., Johnson, M. B.,
1075 Wang, P. P., Sejourne, G. M., Nagy, M. A., Pollina, E. A., Sousa, A. M. M., Shin, T.,
1076 Kenny, C. J., Scotellaro, J. L., Debo, B. M., Gonzalez, D. M., Rento, L. M., Yeh, R. C.,
1077 Song, J. H. T., … Walsh, C. A. (2021). Rewiring of human neurodevelopmental gene
1078 regulatory programs by human accelerated regions. *Neuron*, *109* (20), 3239-3251.e7.
1079 https://doi.org/10.1016/j.neuron.2021.08.005
1080 Gokhman, D., Agoglia, R. M., Kinnebrew, M., Gordon, W., Sun, D., Bajpai, V. K., Naqvi, S.,
1081 Chen, C., Chan, A., Chen, C., Petrov, D. A., Ahituv, N., Zhang, H., Mishina, Y.,
1082 Wysocka, J., Rohatgi, R., & Fraser, H. B. (2021). Human–chimpanzee fused cells reveal
1083 cis-regulatory divergence underlying skeletal evolution. *Nature Genetics*, *53* (4), 467–
1084 476. https://doi.org/10.1038/s41588-021-00804-3
1085 GTEx Consortium. (2017). Genetic effects on gene expression across human tissues. *Nature*,
1086 *550* (7675), 204–213. https://doi.org/10.1038/nature24277
1087 Horlbeck, M. A., Gilbert, L. A., Villalta, J. E., Adamson, B., Pak, R. A., Chen, Y., Fields, A. P.,
1088 Park, C. Y., Corn, J. E., Kampmann, M., & Weissman, J. S. (2016). Compact and highly
1089 active next-generation libraries for CRISPR-mediated gene repression and activation.
1090 *ELife*, *5*, e19760. https://doi.org/10.7554/eLife.19760

1091 Hu, C. K., York, R. A., Metz, H. C., Bedford, N. L., Fraser, H. B., & Hoekstra, H. E. (2022). Cis-
1092 Regulatory changes in locomotor genes are associated with the evolution of burrowing
1093 behavior. *Cell Reports*, *38* (7), 110360. https://doi.org/10.1016/j.celrep.2022.110360
1094 Huang, E. J., & Reichardt, L. F. (2001). Neurotrophins: Roles in neuronal development and
1095 function. *Annual Review of Neuroscience*, *24*, 677–736.
1096 https://doi.org/10.1146/annurev.neuro.24.1.677
1097 Hubisz, M. J., & Pollard, K. S. (2014). Exploring the genesis and functions of Human
1098 Accelerated Regions sheds light on their role in human evolution. *Current Opinion in*
1099 *Genetics & Development*, *29*, 15–21. https://doi.org/10.1016/j.gde.2014.07.005
1100 Ichim, G., Tauszig-Delamasure, S., & Mehlen, P. (2012). Neurotrophins and cell death.
1101 *Experimental Cell Research*, *318* (11), 1221–1228.
1102 https://doi.org/10.1016/j.yexcr.2012.03.006
1103 Jain, A., & Tuteja, G. (2019). TissueEnrich: Tissue-specific gene enrichment analysis.
1104 *Bioinformatics (Oxford, England)*, *35* (11), 1966–1967.
1105 https://doi.org/10.1093/bioinformatics/bty890
1106 John St. John. (n.d.). *SeqPrep*.
1107 Kanton, S., Boyle, M. J., He, Z., Santel, M., Weigert, A., Sanchís-Calleja, F., Guijarro, P., Sidow,
1108 L., Fleck, J. S., Han, D., Qian, Z., Heide, M., Huttner, W. B., Khaitovich, P., Pääbo, S.,
1109 Treutlein, B., & Camp, J. G. (2019). Organoid single-cell genomic atlas uncovers human-
1110 specific features of brain development. *Nature*, *574* (7778), 418–422.
1111 https://doi.org/10.1038/s41586-019-1654-9
1112 Ke, K., Song, Y., Shen, J., Niu, M., Zhang, H., Yuan, D., Ni, H., Zhang, Y., Liu, X., Dai, A., &
1113 Cao, M. (2015). Up-Regulation of Glis2 Involves in Neuronal Apoptosis After
1114 Intracerebral Hemorrhage in Adult Rats. *Cellular and Molecular Neurobiology*, *35* (3),
1115 345–354. https://doi.org/10.1007/s10571-014-0130-1

Kelley, J. L., & Gilad, Y. (2020). Effective study design for comparative functional genomics. *Nature Reviews Genetics*, *21* (7), 385–386. https://doi.org/10.1038/s41576-020-0242-z

King, M.-C., & Wilson, A. C. (1975). Evolution at Two Levels in Humans and Chimpanzees: Their macromolecules are so alike that regulatory mutations may account for their biological differences. *Science*, *188* (4184), 107–116. https://doi.org/10.1126/science.1090005

Korsunsky, I., Millard, N., Fan, J., Slowikowski, K., Zhang, F., Wei, K., Baglaenko, Y., Brenner, M., Loh, P., & Raychaudhuri, S. (2019). Fast, sensitive and accurate integration of single-cell data with Harmony. *Nature Methods*, *16* (12), 1289–1296. https://doi.org/10.1038/s41592-019-0619-0

Korytnikov, R., & Nostro, M. C. (2016). Generation of polyhormonal and multipotent pancreatic progenitor lineages from human pluripotent stem cells. *Methods*, *101*, 56–64. https://doi.org/10.1016/j.ymeth.2015.10.017

Kozlenkov, A., Vermunt, M. W., Apontes, P., Li, J., Hao, K., Sherwood, C. C., Hof, P. R., Ely, J. J., Wegner, M., Mukamel, E. A., Creyghton, M. P., Koonin, E. V., & Dracheva, S. (2020). Evolution of regulatory signatures in primate cortical neurons at cell-type resolution. *Proceedings of the National Academy of Sciences*, *117* (45), 28422–28432. https://doi.org/10.1073/pnas.2011884117

Kuhn, R. M., Haussler, D., & Kent, W. J. (2013). The UCSC genome browser and associated tools. *Briefings in Bioinformatics*, *14* (2), 144–161. https://doi.org/10.1093/bib/bbs038

Langmead, B., & Salzberg, S. L. (2012). Fast gapped-read alignment with Bowtie 2. *Nature Methods*, *9* (4), 357–359. https://doi.org/10.1038/nmeth.1923

Li, H., Handsaker, B., Wysoker, A., Fennell, T., Ruan, J., Homer, N., Marth, G., Abecasis, G., Durbin, R., & 1000 Genome Project Data Processing Subgroup. (2009). The Sequence Alignment/Map format and SAMtools. *Bioinformatics (Oxford, England)*, *25* (16), 2078–2079. https://doi.org/10.1093/bioinformatics/btp352

1142 Liang, D., Elwell, A. L., Aygün, N., Krupa, O., Wolter, J. M., Kyere, F. A., Lafferty, M. J., Cheek,
1143 K. E., Courtney, K. P., Yusupova, M., Garrett, M. E., Ashley-Koch, A., Crawford, G. E.,
1144 Love, M. I., de la Torre-Ubieta, L., Geschwind, D. H., & Stein, J. L. (2021). Cell-type-
1145 specific effects of genetic variation on chromatin accessibility during human neuronal
1146 differentiation. *Nature Neuroscience*, *24* (7), 941–953. https://doi.org/10.1038/s41593-
1147 021-00858-w
1148 Lopez-Delisle, L., Rabbani, L., Wolff, J., Bhardwaj, V., Backofen, R., Grüning, B., Ramírez, F., &
1149 Manke, T. (2021). pyGenomeTracks: Reproducible plots for multivariate genomic
1150 datasets. *Bioinformatics (Oxford, England)*, *37* (3), 422–423.
1151 https://doi.org/10.1093/bioinformatics/btaa692
1152 Love, M. I., Huber, W., & Anders, S. (2014). Moderated estimation of fold change and
1153 dispersion for RNA-seq data with DESeq2. *Genome Biology*, *15* (12), 550.
1154 https://doi.org/10.1186/s13059-014-0550-8
1155 Ma, S., Skarica, M., Li, Q., Xu, C., Risgaard, R. D., Tebbenkamp, A. T. N., Mato-Blanco, X.,
1156 Kovner, R., Krsnik, Ž., de Martin, X., Luria, V., Martí-Pérez, X., Liang, D., Karger, A.,
1157 Schmidt, D. K., Gomez-Sanchez, Z., Qi, C., Gobeske, K. T., Pochareddy, S., … Sestan,
1158 N. (2022). Molecular and cellular evolution of the primate dorsolateral prefrontal cortex.
1159 *Science*, eabo7257. https://doi.org/10.1126/science.abo7257
1160 Mack, K. L., & Nachman, M. W. (2017). Gene Regulation and Speciation. *Trends in Genetics*,
1161 *33* (1), 68–80. https://doi.org/10.1016/j.tig.2016.11.003
1162 Mallanna, S. K., & Duncan, S. A. (2013). Differentiation of hepatocytes from pluripotent stem
1163 cells. *Current Protocols in Stem Cell Biology*, *26*, 1G.4.1-1G.4.13.
1164 https://doi.org/10.1002/9780470151808.sc01g04s26
1165 Maury, Y., Côme, J., Piskorowski, R. A., Salah-Mohellibi, N., Chevaleyre, V., Peschanski, M.,
1166 Martinat, C., & Nedelec, S. (2015). Combinatorial analysis of developmental cues

1167 efficiently converts human pluripotent stem cells into multiple neuronal subtypes. *Nature*
1168 *Biotechnology*, *33* (1), 89–96. https://doi.org/10.1038/nbt.3049
1169 Meisler, M. H., Hill, S. F., & Yu, W. (2021). Sodium channelopathies in neurodevelopmental
1170 disorders. *Nature Reviews Neuroscience*, *22* (3), 152–166.
1171 https://doi.org/10.1038/s41583-020-00418-4
1172 Milani, P., Escalante-Chong, R., Shelley, B. C., Patel-Murray, N. L., Xin, X., Adam, M.,
1173 Mandefro, B., Sareen, D., Svendsen, C. N., & Fraenkel, E. (2016). Cell freezing protocol
1174 suitable for ATAC-Seq on motor neurons derived from human induced pluripotent stem
1175 cells. *Scientific Reports*, *6*, 25474. https://doi.org/10.1038/srep25474
1176 Mizuguchi, R., Kriks, S., Cordes, R., Gossler, A., Ma, Q., & Goulding, M. (2006). Ascl1 and
1177 Gsh1/2 control inhibitory and excitatory cell fate in spinal sensory interneurons. *Nature*
1178 *Neuroscience*, *9* (6), 770–778. https://doi.org/10.1038/nn1706
1179 Montaigne, D., Butruille, L., & Staels, B. (2021). PPAR control of metabolism and cardiovascular
1180 functions. *Nature Reviews Cardiology*, *18* (12), 809–823. https://doi.org/10.1038/s41569-
1181 021-00569-6
1182 Mueller, Fabian. (n.d.). *ChrAccR*.
1183 Naito, Y., Lee, A. K., & Takahashi, H. (2017). Emerging roles of the neurotrophin receptor TrkC
1184 in synapse organization. *Neuroscience Research*, *116*, 10–17.
1185 https://doi.org/10.1016/j.neures.2016.09.009
1186 Netherlands Brain Bank, Vermunt, M. W., Tan, S. C., Castelijns, B., Geeven, G., Reinink, P., de
1187 Bruijn, E., Kondova, I., Persengiev, S., Bontrop, R., Cuppen, E., de Laat, W., &
1188 Creyghton, M. P. (2016). Epigenomic annotation of gene regulatory alterations during
1189 evolution of the primate brain. *Nature Neuroscience*, *19* (3), 494–503.
1190 https://doi.org/10.1038/nn.4229
1191 Pavlovic, B. J., Blake, L. E., Roux, J., Chavarria, C., & Gilad, Y. (2018). A Comparative
1192 Assessment of Human and Chimpanzee iPSC-derived Cardiomyocytes with Primary

Heart Tissues. *Scientific Reports*, *8* (1), 15312. https://doi.org/10.1038/s41598-018-33478-9

Pollard, K. S., Salama, S. R., Lambert, N., Lambot, M.-A., Coppens, S., Pedersen, J. S., Katzman, S., King, B., Onodera, C., Siepel, A., Kern, A. D., Dehay, C., Igel, H., Ares, M., Vanderhaeghen, P., & Haussler, D. (2006). An RNA gene expressed during cortical development evolved rapidly in humans. *Nature*, *443* (7108), 167–172. https://doi.org/10.1038/nature05113

Prud'homme, B., Gompel, N., & Carroll, S. B. (2007). Emerging principles of regulatory evolution. *Proceedings of the National Academy of Sciences*, *104* (suppl_1), 8605–8612. https://doi.org/10.1073/pnas.0700488104

Quinlan, A. R., & Hall, I. M. (2010). BEDTools: A flexible suite of utilities for comparing genomic features. *Bioinformatics (Oxford, England)*, *26* (6), 841–842. https://doi.org/10.1093/bioinformatics/btq033

Ramírez, F., Dündar, F., Diehl, S., Grüning, B. A., & Manke, T. (2014). deepTools: A flexible platform for exploring deep-sequencing data. *Nucleic Acids Research*, *42* (Web Server issue), W187-191. https://doi.org/10.1093/nar/gku365

Reilly, S. K., & Noonan, J. P. (2016). Evolution of Gene Regulation in Humans. *Annual Review of Genomics and Human Genetics*, *17*, 45–67. https://doi.org/10.1146/annurev-genom-090314-045935

Romero, I. G., Ruvinsky, I., & Gilad, Y. (2012). Comparative studies of gene expression and the evolution of gene regulation. *Nature Reviews Genetics*, *13* (7), 505–516. https://doi.org/10.1038/nrg3229

Sharma, R., Khristov, V., Rising, A., Jha, B. S., Dejene, R., Hotaling, N., Li, Y., Stoddard, J., Stankewicz, C., Wan, Q., Zhang, C., Campos, M. M., Miyagishima, K. J., McGaughey, D., Villasmil, R., Mattapallil, M., Stanzel, B., Qian, H., Wong, W., … Bharti, K. (2019). Clinical-grade stem cell-derived retinal pigment epithelium patch rescues retinal

degeneration in rodents and pigs. *Science Translational Medicine*, *11* (475), eaat5580. https://doi.org/10.1126/scitranslmed.aat5580

Shave, R. E., Lieberman, D. E., Drane, A. L., Brown, M. G., Batterham, A. M., Worthington, S., Atencia, R., Feltrer, Y., Neary, J., Weiner, R. B., Wasfy, M. M., & Baggish, A. L. (2019). Selection of endurance capabilities and the trade-off between pressure and volume in the evolution of the human heart. *Proceedings of the National Academy of Sciences*, *116* (40), 19905–19910. https://doi.org/10.1073/pnas.1906902116

Song, J. H. T., Grant, R. L., Behrens, V. C., Kučka, M., Roberts Kingman, G. A., Soltys, V., Chan, Y. F., & Kingsley, D. M. (2021). Genetic studies of human-chimpanzee divergence using stem cell fusions. *Proceedings of the National Academy of Sciences of the United States of America*, *118* (51), e2117557118. https://doi.org/10.1073/pnas.2117557118

Starr, A. L., Gokhman, D., & Fraser, H. B. (2023). Accounting for cis-regulatory constraint prioritizes genes likely to affect species-specific traits. *Genome Biology*, *24* (1), 11. https://doi.org/10.1186/s13059-023-02846-8

Storey Lab. (n.d.). *Qvalue*.

Subramanian, A., Tamayo, P., Mootha, V. K., Mukherjee, S., Ebert, B. L., Gillette, M. A., Paulovich, A., Pomeroy, S. L., Golub, T. R., Lander, E. S., & Mesirov, J. P. (2005). Gene set enrichment analysis: A knowledge-based approach for interpreting genome-wide expression profiles. *Proceedings of the National Academy of Sciences*, *102* (43), 15545–15550. https://doi.org/10.1073/pnas.0506580102

Su-Feher, L., Rubin, A. N., Silberberg, S. N., Catta-Preta, R., Lim, K. J., Ypsilanti, A. R., Zdilar, I., McGinnis, C. S., McKinsey, G. L., Rubino, T. E., Hawrylycz, M. J., Thompson, C., Gartner, Z. J., Puelles, L., Zeng, H., Rubenstein, J. L. R., & Nord, A. S. (2022). Single cell enhancer activity distinguishes GABAergic and cholinergic lineages in embryonic mouse basal ganglia. *Proceedings of the National Academy of Sciences*, *119* (15), e2108760119. https://doi.org/10.1073/pnas.2108760119

Sullivan, P. F., Meadows, J. R. S., Gazal, S., Phan, B. N., Li, X., Genereux, D. P., Dong, M. X., Bianchi, M., Andrews, G., Sakthikumar, S., Nordin, J., Roy, A., Christmas, M. J., Marinescu, V. D., Wallerman, O., Xue, J. R., Li, Y., Yao, S., Sun, Q., … Lindblad-Toh, K. (2023). *Leveraging Base Pair Mammalian Constraint to Understand Genetic Variation and Human Disease* [Preprint]. Genomics. https://doi.org/10.1101/2023.03.10.531987

Traag, V. A., Waltman, L., & van Eck, N. J. (2019). From Louvain to Leiden: Guaranteeing well-connected communities. *Scientific Reports*, *9* (1), 5233. https://doi.org/10.1038/s41598-019-41695-z

Trevino, A. E., Sinnott-Armstrong, N., Andersen, J., Yoon, S.-J., Huber, N., Pritchard, J. K., Chang, H. Y., Greenleaf, W. J., & Pașca, S. P. (2020). Chromatin accessibility dynamics in a model of human forebrain development. *Science (New York, N.Y.)*, *367* (6476), eaay1645. https://doi.org/10.1126/science.aay1645

Trizzino, M., Park, Y., Holsbach-Beltrame, M., Aracena, K., Mika, K., Caliskan, M., Perry, G. H., Lynch, V. J., & Brown, C. D. (2017). Transposable elements are the primary source of novelty in primate gene regulation. *Genome Research*, *27* (10), 1623–1633. https://doi.org/10.1101/gr.218149.116

van de Geijn, B., McVicker, G., Gilad, Y., & Pritchard, J. K. (2015). WASP: Allele-specific software for robust molecular quantitative trait locus discovery. *Nature Methods*, *12* (11), 1061–1063. https://doi.org/10.1038/nmeth.3582

Vanderhaeghen, P., & Polleux, F. (2023). Developmental mechanisms underlying the evolution of human cortical circuits. *Nature Reviews Neuroscience*, *24* (4), 213–232. https://doi.org/10.1038/s41583-023-00675-z

Vierstra, J., Lazar, J., Sandstrom, R., Halow, J., Lee, K., Bates, D., Diegel, M., Dunn, D., Neri, F., Haugen, E., Rynes, E., Reynolds, A., Nelson, J., Johnson, A., Frerker, M., Buckley, M., Kaul, R., Meuleman, W., & Stamatoyannopoulos, J. A. (2020). Global reference

mapping of human transcription factor footprints. *Nature*, *583* (7818), 729–736. https://doi.org/10.1038/s41586-020-2528-x

Vu, H., & Ernst, J. (2022). Universal annotation of the human genome through integration of over a thousand epigenomic datasets. *Genome Biology*, *23* (1), 9. https://doi.org/10.1186/s13059-021-02572-z

Wang, B., & Tontonoz, P. (2018). Liver X receptors in lipid signalling and membrane homeostasis. *Nature Reviews Endocrinology*, *14* (8), 452–463. https://doi.org/10.1038/s41574-018-0037-x

Watanabe, A., Toyota, T., Owada, Y., Hayashi, T., Iwayama, Y., Matsumata, M., Ishitsuka, Y., Nakaya, A., Maekawa, M., Ohnishi, T., Arai, R., Sakurai, K., Yamada, K., Kondo, H., Hashimoto, K., Osumi, N., & Yoshikawa, T. (2007). Fabp7 Maps to a Quantitative Trait Locus for a Schizophrenia Endophenotype. *PLoS Biology*, *5* (11), e297. https://doi.org/10.1371/journal.pbio.0050297

Wittkopp, P. J., Haerum, B. K., & Clark, A. G. (2004). Evolutionary changes in cis and trans gene regulation. *Nature*, *430* (6995), 85–88. https://doi.org/10.1038/nature02698

Wittkopp, P. J., & Kalay, G. (2012). Cis-regulatory elements: Molecular mechanisms and evolutionary processes underlying divergence. *Nature Reviews Genetics*, *13* (1), 59–69. https://doi.org/10.1038/nrg3095

Wolf, F. A., Angerer, P., & Theis, F. J. (2018). SCANPY: Large-scale single-cell gene expression data analysis. *Genome Biology*, *19* (1), 15. https://doi.org/10.1186/s13059-017-1382-0

Wolf, F. A., Hamey, F. K., Plass, M., Solana, J., Dahlin, J. S., Göttgens, B., Rajewsky, N., Simon, L., & Theis, F. J. (2019). PAGA: Graph abstraction reconciles clustering with trajectory inference through a topology preserving map of single cells. *Genome Biology*, *20* (1), 59. https://doi.org/10.1186/s13059-019-1663-x

Yang, N., Chanda, S., Marro, S., Ng, Y.-H., Janas, J. A., Haag, D., Ang, C. E., Tang, Y., Flores, Q., Mall, M., Wapinski, O., Li, M., Ahlenius, H., Rubenstein, J. L., Chang, H. Y., Buylla, A. A., Südhof, T. C., & Wernig, M. (2017). Generation of pure GABAergic neurons by transcription factor programming. *Nature Methods*, *14* (6), 621–628. https://doi.org/10.1038/nmeth.4291

Yao, Z., van Velthoven, C. T. J., Nguyen, T. N., Goldy, J., Sedeno-Cortes, A. E., Baftizadeh, F., Bertagnolli, D., Casper, T., Chiang, M., Crichton, K., Ding, S.-L., Fong, O., Garren, E., Glandon, A., Gouwens, N. W., Gray, J., Graybuck, L. T., Hawrylycz, M. J., Hirschstein, D., … Zeng, H. (2021). A taxonomy of transcriptomic cell types across the isocortex and hippocampal formation. *Cell*, *184* (12), 3222-3241.e26. https://doi.org/10.1016/j.cell.2021.04.021

York, R. A., Patil, C., Abdilleh, K., Johnson, Z. V., Conte, M. A., Genner, M. J., McGrath, P. T., Fraser, H. B., Fernald, R. D., & Streelman, J. T. (2018). Behavior-dependent *cis* regulation reveals genes and pathways associated with bower building in cichlid fishes. *Proceedings of the National Academy of Sciences*, *115* (47). https://doi.org/10.1073/pnas.1810140115

Yu, X., Lin, J., Zack, D. J., & Qian, J. (2006). Computational analysis of tissue-specific combinatorial gene regulation: Predicting interaction between transcription factors in human tissues. *Nucleic Acids Research*, *34* (17), 4925–4936. https://doi.org/10.1093/nar/gkl595

Zhang, S., Zhang, H., Zhou, Y., Qiao, M., Zhao, S., Kozlova, A., Shi, J., Sanders, A. R., Wang, G., Luo, K., Sengupta, S., West, S., Qian, S., Streit, M., Avramopoulos, D., Cowan, C. A., Chen, M., Pang, Z. P., Gejman, P. V., … Duan, J. (2020). Allele-specific open chromatin in human iPSC neurons elucidates functional disease variants. *Science*, *369* (6503), 561–565. https://doi.org/10.1126/science.aay3983

Zhang, Y., Liu, T., Meyer, C. A., Eeckhoute, J., Johnson, D. S., Bernstein, B. E., Nusbaum, C., Myers, R. M., Brown, M., Li, W., & Liu, X. S. (2008). Model-based analysis of ChIP-Seq (MACS). *Genome Biology*, *9* (9), R137. https://doi.org/10.1186/gb-2008-9-9-r137

Zhu, A., Ibrahim, J. G., & Love, M. I. (2019). Heavy-tailed prior distributions for sequence count data: Removing the noise and preserving large differences. *Bioinformatics*, *35* (12), 2084–2092. https://doi.org/10.1093/bioinformatics/bty895